BULGARIAN ACADEMY OF SCIENCES
Institute of Biophysics and Biomedical Engineering
Department “Lipid-protein interactions”

Dayana Slavchova Benkova

BIOLOGICAL ACTIVITY OF CHITOSAN-BASED NANOMATERIALS

SYNOPSIS OF THE PhD THESIS

for awarding the educational and scientific degree
“DOCTOR”
Higher education area
“Natural sciences, mathematics and informatics”
Professional field *“Biological sciences”*
PhD programme *“Biophysics”*

Research supervisors:
Prof. Galya Staneva, PhD
Assoc. Prof. Aneliya Kostadinova

Sofia, 2026

The Ph.D. thesis contains 149 pages with 59 figures. The cited literature contains 182 sources.

The experimental work was primarily carried out in the laboratories of the Department of Lipid–Protein Interactions at the Institute of Biophysics and Biomedical Engineering, Bulgarian Academy of Sciences (BAS).

The microbiological studies were conducted in the laboratories of the Department of Mycology at the Stephan Angeloff Institute of Microbiology, BAS, with the assistance of Assoc. Prof. Dr. Ekaterina Krumova and her research team.

The investigated nanomaterials were synthesized, characterized, and provided by Dr. Hisham Elshoky and his research team from the Central Laboratory for Nanotechnology and Advanced Materials and the Regional Center for Food and Feed at the Agricultural Research Center, Giza, Egypt.

The PhD thesis was presented and discussed at a meeting of an extended scientific seminar of the Department "Lipid-protein interactions" at the Institute of Biophysics and Biomedical Engineering - BAS, held on 07.04.2026.

Contents:

Abbreviations

AA - acetic acid
Chol - cholesterol
CS - chitosan
DLS - dynamic light scattering
DI-H_2O – deionized water
ddH_2O – double distilled water
EggPC - egg phosphatidylcholine
EggSM - egg sphingomyelin
ELS - electrophoretic light scattering
GP - general polarization
GUVs - giant unilamellar vesicles
HNCs - hybrid nanocomposites
HRTEM - high resolution transmissive electron microscopy
L_d - liquid disordered
L_o - liquid ordered
LUVs - large unilamellar vesicles
MDA - malondialdehyde
NMs - nanomaterials
NPs - nanoparticles
OS - oxidative stress
PC - phosphatidylcholine
PCC - protein carbonyl content
PEG - polyethylene glycol
ROS - reactive oxygen species
SOD - superoxide dismutase

I. Introduction

Nanotechnology is one of the most rapidly advancing fields in modern science and industry. The value of nanomaterials lies in their small size, high surface-to-volume ratio, reactive surface, and morphology. These characteristics impart distinctive physicochemical properties, enabling a wide range of potential applications. Contemporary research is focused on the development of increasingly complex hybrid nanocomposites with both organic and inorganic components, aimed at enhancing their properties and functional activities. As organic components, various polymers are frequently employed, such as the synthetic polyethylene glycol and the semi-synthetic chitosan, due to their excellent biocompatibility, low toxicity, and low immunogenicity. Their combination with an inorganic phase—often bioactive metal oxides—represents a targeted strategy for achieving synergistic properties and enhanced activity across applications ranging from biomedicine to agriculture.

Hybrid nanomaterials containing chitosan or polyethylene glycol in combination with inorganic oxides such as ZnO, CuO, and SiO_2 are regarded as promising materials with biomedical applications, including diagnostics, systems for controlled delivery of bioactive substances, and anticancer therapies. Their effectiveness in terms of cellular uptake and internalization is closely related to the way these nanomaterials interact with the cell membrane. Cell membranes are complex and heterogeneous structures in terms of their lipid and protein composition. However, many studies focus primarily on protein components, often underestimating the role of the lipid bilayer in the processes of interaction and uptake of nanomaterials by cells. Lipids are a fundamental structural and functional component of biological membranes, forming various lipid–protein domains with specific size, lipid composition, and phase state. Direct interactions between nanomaterials and lipid molecules, as well as different lipid phases, may induce changes in the biophysical and physicochemical characteristics of the membrane bilayer. The analysis of these changes can be used to elucidate key mechanisms related to cellular uptake, membrane penetration, degree of biocompatibility, and the relationship between nanomaterial characteristics and their effectiveness. Based on the above, one of the objectives of the present doctoral dissertation is formulated, namely to elucidate the fundamental principles of interaction between chitosan-based and polyethylene glycol-based hybrid nanocomposites containing ZnO, CuO, and SiO_2, and membrane models that reproduce both the lipid composition and the three main phase states of the cell membrane—liquid-disordered (L_d), liquid-ordered (L_o), and phase coexistence (L_d/L_o). Understanding these mechanisms provides a basis for the targeted optimization of nanomaterials as "smart" drug delivery systems with minimal nanotoxicity.

In addition to biomedicine, such polymer-based hybrid nanocomposites have promising applications in agriculture as effective and environmentally compatible nanopesticides. Modern agriculture faces serious challenges related to the increasing resistance of phytopathogens and the widespread use of synthetic, often toxic pesticides. These issues necessitate the development of new, environmentally sustainable solutions. In this context, chitosan-based hybrid nanocomposites with CuO,

ZnO, and SiO_2 are considered promising candidates for nano pesticides. Both chitosan and inorganic oxides exhibit pronounced antifungal activity, and their combination into hybrid systems represents an innovative approach to enhancing effectiveness. Based on this, the second objective of the present dissertation is aimed at evaluating the pesticide-like activity of chitosan-based hybrid nanocomposites with ZnO, CuO, and SiO_2 against some of the most important phytopathogens in agriculture, namely *Alternaria solani* and *Fusarium solani*. These pathogens are among the main causes of significant losses in crops such as tomatoes, potatoes, and soybeans, both during vegetation and post-harvest. Investigating the membrane-damaging and pro-oxidant mechanisms of action of antifungal nanomaterials may provide a scientific basis for the development of sustainable and environmentally friendly nano pesticides in modern agriculture.

II. Aims and Objectives

First Aim: To elucidate the principles of interaction between chitosan-based and polyethylene-based hybrid nanocomposites and membrane models mimicking the lipid phase heterogeneity of eukaryotic membranes.

To achieve the first aim, the following objectives were defined:

- **Task 1:** Formation of large unilamellar vesicles (LUVs) composed of single-, binary-, and ternary-component lipid mixtures using the extrusion method. Investigation of changes in lipid ordering in liquid-disordered (L_d), liquid-ordered (L_o), and L_d/L_o phase coexistence induced by nanomaterials (NMs) using Laurdan fluorescence spectroscopy.
- **Task 2:** Investigation of changes in the colloidal characteristics of LUVs treated with NMs using dynamic light scattering (DLS) and electrophoretic light scattering (ELS). Determination of NM-induced changes in surface charge, mean size, and polydispersity of LUVs.
- **Task 3:** Formation of giant unilamellar vesicles (GUVs) from single- and ternary-component lipid mixtures using the electroformation method. Observation of NM-induced morphological changes in L_d and L_d/L_o vesicles by phase-contrast and fluorescence microscopy.

Second Aim: To investigate the antifungal activity of chitosan-based hybrid nanocomposites containing ZnO, CuO, and SiO_2 against some of the most important phytopathogenic fungi—*Alternaria solani* and *Fusarium solani*.

To achieve the second aim, the following objectives were defined:

- **Task 1:** Microbiological evaluation of the antifungal activity of chitosan-based hybrid nanocomposites against *A. solani* and *F. solani* using the agar diffusion method. Visual assessment of inhibition zones and determination of antifungal activity.
- **Task 2:** Evaluation of the prooxidant activity of the tested chitosan-based hybrid nanocomposites. Measurement of oxidative stress levels in fungal cells after treatment through quantification of oxidative stress biomarkers.
- **Task 3:** Investigation of quantitative changes in lipid ordering in fungal cell membranes after treatment with chitosan-based hybrid nanocomposites using Laurdan fluorescence spectroscopy.

III. Methods Used

1. Preparation if nanomaterial dispersions

1.1. Preparation of nanomaterial dispersions for model membrane systems in 1% acetic acid (AA) in double-distilled water (ddH_2O)

1.2. Preparation of nanomaterial dispersions for phytopathogenic fungi in 0.2% dimethyl sulfoxide (DMSO).

2. Formation of large unilamellar vesicles (LUVs) using the extrusion method. Formation of LUVs from four different lipid mixtures: egg phosphatidylcholine (EggPC) for L_d phase; EggPC and cholesterol (Chol) (1/1) for L_o phase; egg sphingomyelin (EggSM) and Chol (1/1) for raft-like L_o phase, and EggPC/EggSM/Chol (2/1/1) for L_d/L_o phase coexistence.

3. Formation of giant unilamellar vesicles (GUVs) using electroformation. Formation of GUVs using two different lipid mixtures: EggPC for L_d phase and EggPC/EggSM/Chol (2/1/1) for L_d/L_o phase coexistence.

4. Laurdan fluorescence spectroscopy.

5. Light scattering techniques: Dynamic light scattering (DLS) and Electrophoretic light scattering (ELS).

6. Optical microscopy: Phase-contrast microscopy and Fluorescence microscopy.

7. Agar diffusion method.

8. Spectrophotometric determination of oxidative stress markers via absorbance measurements:

8.1. Determination of superoxide dismutase (SOD) activity using the Lowry method and Nitro Blue Tetrazolium (NBT) assay.

8.2. Determination of malondialdehyde (MDA) levels using a thiobarbituric acid (TBA) lipid peroxidation assay kit.

8.3. Determination of protein carbonyl content (PCC) using a 2,4-dinitrophenylhydrazine (DNPH)-based assay kit.

9. Statistical analysis: Shapiro–Wilk normality test and one-way ANOVA with Tukey post hoc test.

IV. Results

IV.1. Characteristics of nanomaterials

The colloidal characteristics (average size and ζ-potential values) of the investigated nanomaterials (NMs) were measured using DLS and ELS. The morphology of the NMs was visualized by high-resolution transmission electron microscopy (HRTEM).

IV.1.1. Characteristics of NMs for Model Membranes

The colloidal characteristics were measured in dispersions of NMs in ddH_2O. The obtained DLS profiles showed that chitosan (CS) nanoparticles (NPs) have the smallest average size (hydrodynamic diameter) of 38 nm and the highest ζ-potential value of +33.5 mV (Table 1). Chitosan-based hybrid nanocomposites (HNCs) exhibited the following characteristics: CS–CuO: 334.3 nm and +16.1 mV; CS–SiO_2: 770 nm and +17.7 mV; CS–ZnO: 438 nm and +21.6 mV. A clear trend was observed toward an increase in average hydrodynamic size and a decrease in surface charge upon combining the polymer with the respective metal oxides. The largest size (1116 nm) and the lowest ζ-potential (+9.48 mV) were measured for PEG–ZnO HNCs.

HRTEM images revealed that CS NPs possess a spherical morphology with sizes ranging from 20 to 40 nm (Fig. 1), which corresponds well to the sizes obtained from their DLS profile (Table 1). The hybrid nanocomposites CS–CuO and CS–SiO_2 were visualized as spherical agglomerates formed between the polymer and the oxides, with characteristic sizes of 10–20 nm and 150–200 nm, respectively. For CS–ZnO and PEG–ZnO HNCs, similar sizes of approximately 100 nm and 90 nm were observed (Fig. 1), along with comparable morphology—a ZnO spherical core coated with a polymer layer of CS and PEG, respectively. For all HNCs, a discrepancy between the average sizes obtained from DLS and those observed by HRTEM was noted, which is most likely due to aggregation occurring after their dispersion.

HNCs	ζ – Potential (mV)	DLS Mean Size(nm)	HRTEM Size (nm)
CS NPs	+ 33.5 ± 5.8	38 ± 14	30 ± 9
CS-ZnO HNCs	+ 17.7 ± 7.5	438 ± 7	100 ± 13
CS-CuO HNCs	+ 16.1 ± 4.2	334 ± 25	15 ± 5
CS-SiO_2 HNCs	+ 21.6 ± 7.2	770 ± 10	175 ± 16
PEG-ZnO HNCs	+ 9.5 ± 4.4	1116 ± 12	90 ± 11

Table 1: Characteristics of NM: ζ – potential values; DLS mean sizes и HRTEM sizes.

IV.1.2. Characteristics of CS-Based HNCs for Phytopathogenic Fungi

The colloidal characteristics were measured in dispersions of CS-based HNCs in 0.2% DMSO. The obtained average sizes and ζ-potential values of the HNCs are as follows: CS–ZnO: 167 nm and +22.5 mV; CS–CuO: 65 nm and +21.7 mV; CS–SiO_2: 76 nm and +30 mV (Table 2). HRTEM images revealed that CS–SiO_2 and CS–CuO HNCs are present in the form of spherical agglomerates, with sizes of approximately 85 nm and 55 nm, respectively (Fig. 2). The CS–ZnO HNCs exhibited a specific morphology consisting of an aggregated CS core coated with a ZnO layer, with a characteristic size of approximately 120 nm (Fig. 2).

HNCs	ζ – потенциал (mV)	DLS средни размери (nm)	HRTEM размери (nm)
CS-ZnO HNCs	+ 23.5 ± 5.5	167 ± 6	120 ± 11
CS-CuO HNCs	+ 21.7 ± 7.5	65 ± 4	55 ± 5
CS-SiO_2 HNCs	+ 30 ± 7.2	76 ± 5	85 ± 8

Таблица 2: Характеристики на NMs: стойности на ζ - потенциал, DLS средни размери и HRTEM размери на CS-базираните HNCs.

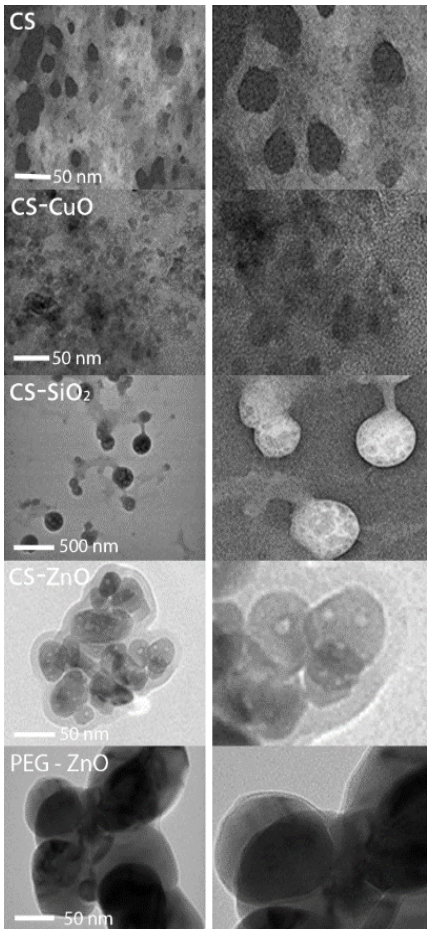

Figure 1: Morphology and size of the NMs visualized with HRTEM.

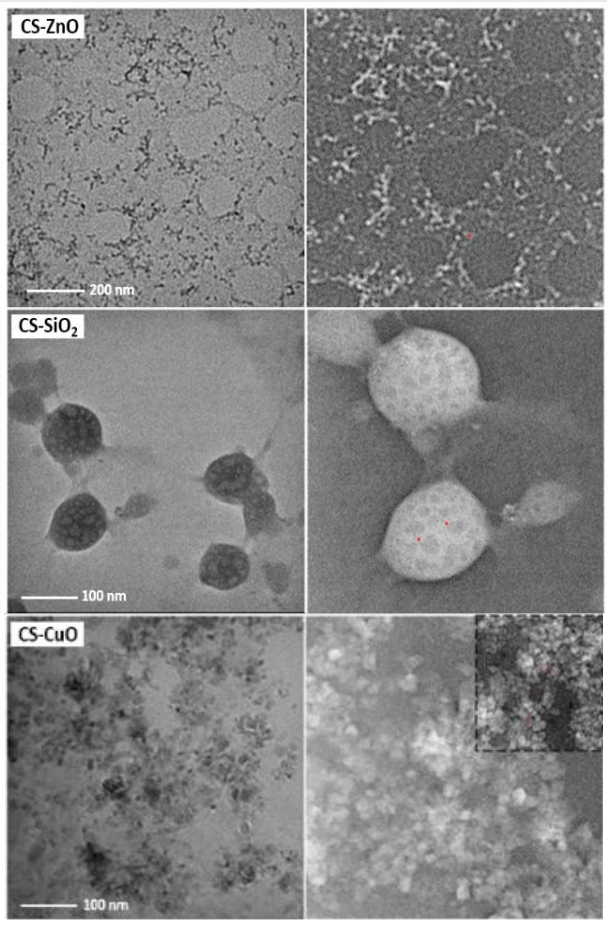

Figure 2: Morphology and size of the CS-based HNCs visualized with HRTEM.

IV.2. Interactions of Nanomaterials with Model Membranes

IV.2.1. Quantitative Changes in Lipid Order of LUVs

IV.2.1.1. Changes in Lipid Order of EggPC LUVs – Model of L_d Phase

Phosphatidylcholine (PC) is a zwitterionic glycerophospholipid and the most abundant lipid species in eukaryotic cell membranes. At physiological temperature, PC forms membranes in the liquid-disordered (L_d) phase due to the presence of a polyunsaturated fatty acid at the *sn*-2 position. To investigate the effect of the NMs on lipid order, Laurdan fluorescence spectroscopy and large unilamellar vesicles (LUVs) were used as membrane models. All tested NMs were added asymmetrically to the LUV dispersions, ensuring that interactions between NMs and vesicles occur at the outer leaflet of the membrane. Figure 3A shows the normalized emission spectrum of Laurdan in untreated egg phosphatidylcholine (EggPC) LUVs (without NMs). Following spectral deconvolution, three emission peaks with different intensities were identified. The Laurdan emission spectrum in EggPC LUVs shows the highest intensity peak centered at 485 nm (green curve), indicating that the lipids are in the L_d phase. Two additional lower-intensity peaks are centered at 422 nm (blue shift) and 518 nm (red shift) (Fig. 3A). These results indicate that the Laurdan molecule is sensitive to at least three distinct microenvironments within the membrane. The fluorophore is localized in the region of the glycerol backbone of the lipids [1,2]. Laurdan fluorescence at different wavelengths reflects different penetration depths within the lipid bilayer: shorter wavelengths correspond to deeper localization within the membrane, whereas longer wavelengths indicate positioning closer to the aqueous interface. Conformational changes in the glycerol backbone, particularly those associated with its hydration, as well as the reorientation of lipid headgroups, depend on the position and orientation of the sn-1 and *sn*-2 fatty acyl chains [1,2]. Figure 3B presents the emission spectrum of EggPC LUVs treated with 0.01 mg/ml CS NPs. A shift toward shorter wavelengths is observed, indicating a decrease in polarity around the glycerol backbone of EggPC and an increase in lipid order in this region of the bilayer.

The control generalized polarization (GP) value of pure EggPC LUVs is negative (−0.1537) (Fig. 4A), confirming that the vesicle bilayer is in the L_d phase. The addition of NMs to EggPC LUVs induces a concentration-dependent increase in GP values (Fig. 4A), indicating enhanced lipid order. The strongest effect is observed for CS NPs, while the weakest is observed for PEG–ZnO HNCs. Since CS-based HNCs were prepared in a 1% aqueous solution of acetic acid (AA), the effect of the acid was tested at equivalent concentrations corresponding to those in the NM/EggPC LUVs dispersions: 0.005 mg/ml (0.005% AA), 0.01 mg/ml (0.01% AA), 0.02 mg/ml (0.02% AA), 0.04 mg/ml (0.04% AA), and 0.08 mg/ml (0.08% AA). It was found that AA also increases lipid order; however, this effect is significantly weaker compared to all tested NMs (Fig. 4A).

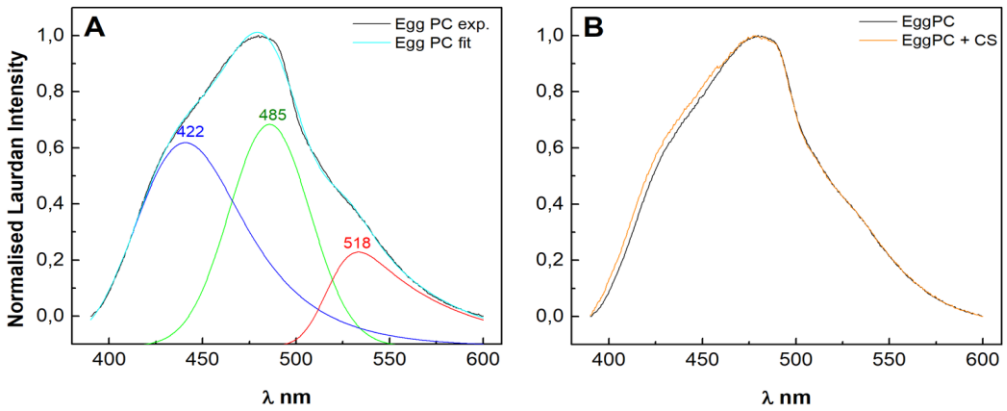

Figure 3: Spectra of untreated EggPC LUVs and CS-treated EggPC LUVs: (A) Deconvolution of the Laurdan spectra (black curve) into three Gaussian peaks – a blue peak at 422 nm, a green peak at 485 nm, and a red peak at 518 nm. The sum of these peaks is shown as a light blue curve. (B) Laurdan spectra of CS-treated EggPC LUVs (0.01 mg/ml) (orange curve), shifted towards the shorter wavelength compared to the control (black curve). This indicates a higher degree of lipid order relative untreatred EggPC LUVs. Measurements were carried out at 37°C.

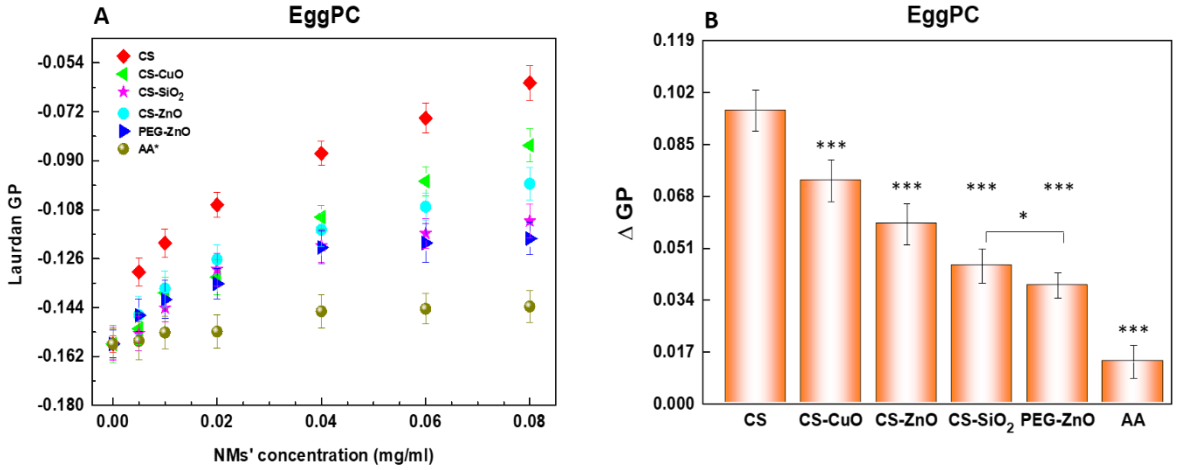

Figure 4: Laurdan GP of EggPC LUVs as a function of NM concentration, measured at 37°C. (A) Negative GP value for EggPC LUVs (−0.1537), indicative of membranes in the Ld phase. A progressive increase in GP values is observed with increasing NM concentration. (B) ΔGP = GP (0.08 mg/mL) − GP (0 mg/mL) represents the quantitative changes depending on the type of NMs. GP values for AA were measured at percentage concentrations equivalent to those in the corresponding EggPC LUVs/NMs dispersions: 0.005, 0.01, 0.02, 0.04, and 0.08% AA (*). Standard deviations (SDs) of GP were obtained from three independent experiments with four measurements per sample. Statistical significance is indicated as follows: *** $p < 0.001$ (when comparing CS NPs with all CS-based HNCs and among CS-based HNCs), * $p < 0.05$ (when comparing CS–SiO_2 with PEG–ZnO HNCs).

Figure 4B presents the quantitative changes in lipid order as a function of the type of tested NMs. The parameter ΔGP represents the difference between the highest GP value (in this case at a concentration of 80 μg/ml) and the control GP value. The quantitative changes in lipid ordering in the Ld phase induced by NMs follow the descending order: CS > CS–CuO > CS–ZnO > CS–SiO_2 > PEG–ZnO. The results from the conducted experiments showed that after incubation of the models with NMs (10 min), the GP values of the NMs/EggPC LUVs dispersions remained unchanged for an additional 20

minutes. Therefore, the obtained GP values (and ΔGP) represent average values for the entire membrane bilayer, encompassing all changes occurring in both the outer and inner leaflets.

IV.2.1.2. Changes in Lipid Ordering of EggSM/Chol LUVs – Model of Raft-Like L_o Phase

The binary mixture of egg sphingomyelin (EggSM) and cholesterol (Chol) in ratio 1/1 is used as a model of the raft-like liquid-ordered (L_o) phase, representing raft-like domains in eukaryotic cell membranes. The control GP value for these models is high and positive (0.5252), reflecting a bilayer with high lipid order and low polarity (Fig. 5A, B, C, and D). For CS NPs and CS-based HNCs, an increase in GP values is observed at concentrations up to 40 μg/ml (Fig. 5A, B, C, and D). At higher concentrations, no significant changes in lipid order of the vesicles are detected. A pronounced concentration-dependent effect is observed only for PEG–ZnO HNCs (Fig. 5C). The hybrid nanocomposite CS–SiO_2 exhibits a distinct interaction pattern with the raft-like L_o phase. At low concentrations (5–10 μg/ml), a slight increase in lipid order is observed. However, with each subsequent increase in CS–SiO_2 concentration, the GP values decrease exponentially, indicating a fluidizing effect of this nanocomposite on the membrane (Fig. 5D).

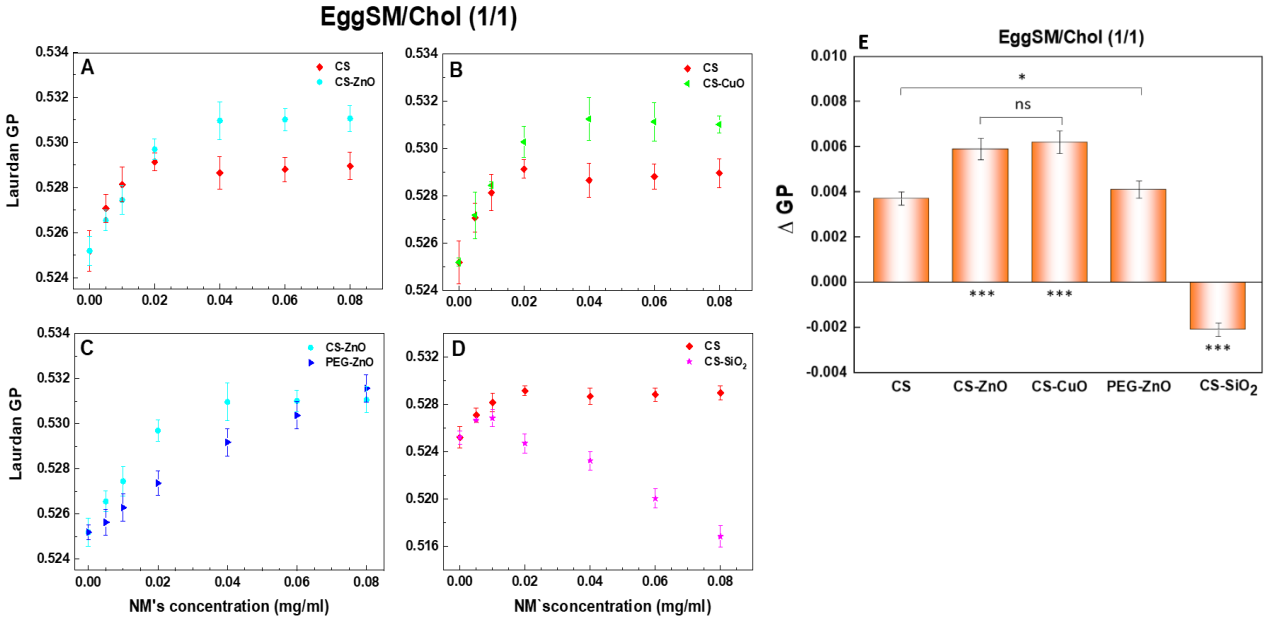

Figure 5: Laurdan GP of EggSM/Chol LUVs as a function of NM concentration, measured at 37°C. The control GP value of EggSM/Chol (1/1) is 0.5252, indicative of membranes in the Lo phase. Comparison of the effects of: A) CS NPs vs. CS–ZnO; B) CS NPs vs. CS–CuO; C) PEG–ZnO vs. CS–ZnO; D) CS NPs vs. CS–SiO_2. E) Laurdan ΔGP of EggSM/Chol (1/1) LUVs as a function of NM type. ΔGP = GP (0.04 mg/mL) − GP (0 mg/mL). Statistical significance is indicated as follows: *** $p < 0.001$ (when comparing CS NPs with CS–ZnO, CS–CuO with CS–SiO_2, CS–ZnO with PEG–ZnO, and PEG–ZnO with CS–SiO_2), * $p < 0.05$ (when comparing CS NPs with PEG–ZnO), "ns" (not significant) indicates no statistically significant difference (when comparing CS NPs with PEG–ZnO).

To quantify the changes in the raft-like L_o phase, ΔGP was calculated as the difference between the GP values at a concentration of 40 μg/ml and the control GP value (Fig. 5E). This concentration was selected because no significant changes were observed above 40 μg/ml. It was found that the quantitative changes in lipid order in the raft-like L_o phase are approximately two times smaller than those observed in the L_d phase (Fig. 5B, Fig. 4). In the raft-like model, the strongest and comparable effects were observed for CS–ZnO and CS–CuO HNCs. The nanocomposite PEG–ZnO and pure CS NPs, in turn, induced weaker changes (Fig. 5E). Only CS–SiO_2 exhibited an opposite effect. For this type of NM, an increase in bilayer polarity was observed, indicating a fluidizing effect. The quantitative changes in lipid order in the raft-like L_o phase induced by NMs follow the descending order: CS–CuO ≈ CS–ZnO > PEG–ZnO > CS > CS–SiO_2.

IV.2.1.3. Changes in Lipid Ordering of EggPC/Chol LUVs – Model of L_o Phase

The binary mixture of EggPC/Chol (1/1) also serves as a model for the formation of a lipid system in the L_o phase. The control GP value of these vesicles is high and positive (0.3293) (Fig. 6A, B, C, and D), indicating that the membrane bilayer is in the L_o phase rather than the L_d phase. Compared to the raft-like L_o phase, the EggPC/Chol L_o phase is less ordered, as reflected by its lower control GP value.

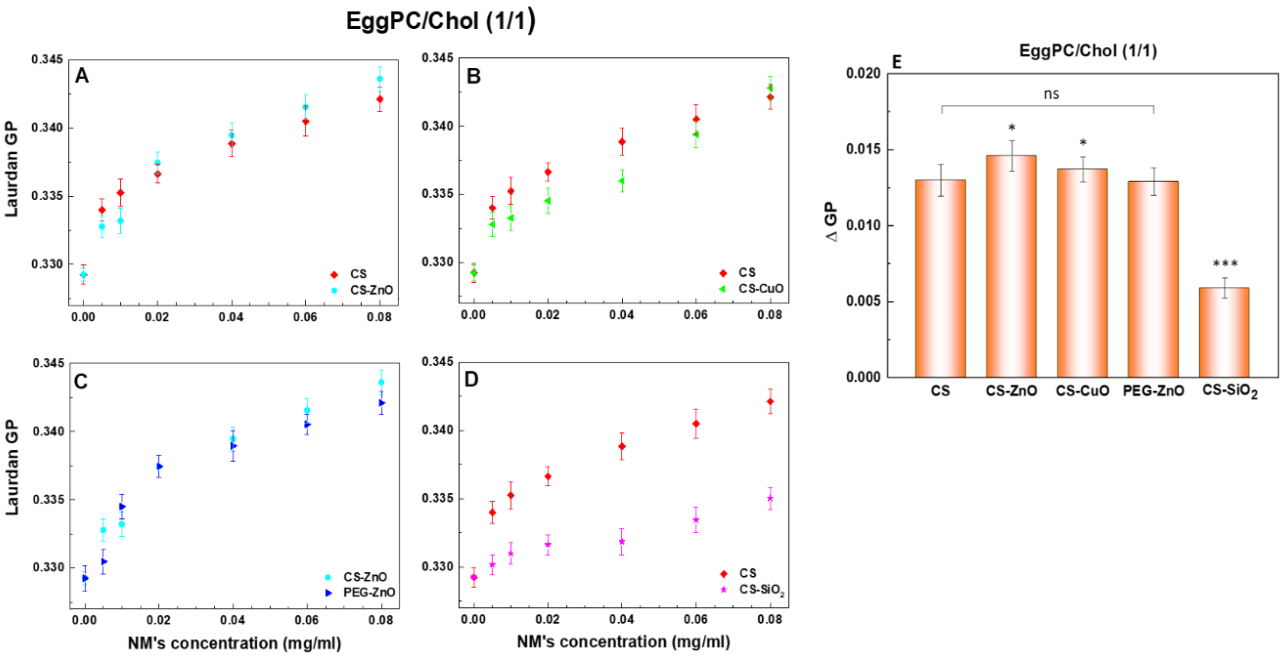

Figure 6: Laurdan GP of EggPC/Chol LUVs as a function of NM concentration, measured at 37°C. The control GP value of EggPC/Chol (1/1) is 0.3293, indicative of membranes in the Lo phase, but with lower lipid ordering compared to the raft-like Lo phase. Comparison of the effects of: A) CS NPs vs. CS–ZnO; B) CS NPs vs. CS–CuO; C) PEG–ZnO vs. CS–ZnO; D) CS NPs vs. CS–SiO_2. E) Laurdan ΔGP of EggPC/Chol (1/1) LUVs as a function of NM type. ΔGP = GP (0.08 mg/mL) − GP (0 mg/mL). Statistical significance is indicated as follows: *** $p < 0.001$ (when comparing CS NPs with CS–SiO_2; CS–ZnO with PEG–ZnO and CS–SiO_2; CS–CuO with PEG–ZnO and CS–SiO_2), * $p < 0.05$ (when comparing CS NPs with CS–ZnO and CS–CuO; CS–ZnO with CS–CuO), and ns (when comparing CS NPs with PEG–ZnO).

In this model, similar to the raft-like L_o phase, the largest quantitative changes are observed for CS–ZnO and CS–CuO, followed by CS NPs, PEG–ZnO, and CS–SiO_2 (Fig. 6E). This indicates that the ordering effect of the nanomaterials (NMs) is not lipid-specific. The quantitative changes in lipid order in the EggPC/Chol L_o phase are five times smaller than those observed in the L_d phase (Fig. 4B) and three times greater than those in the raft-like L_o phase (Fig. 5E). The quantitative changes in lipid order in the EggPC/Chol L_o phase follow the descending order: CS–ZnO > CS–CuO > CS ≈ PEG–ZnO > CS–SiO_2.

IV.2.1.4. Changes in Lipid Order of EggPC/EggSM/Chol LUVs in L_d/L_o Phase Coexistence

The three-component mixture of EggPC/EggSM/Chol in a 2/2/1 ratio was selected as the most suitable model of the eukaryotic plasma membrane in this study due to its lipid composition and phase heterogeneity. At physiological temperature, these vesicles exhibit phase separation in the bilayer, with EggSM and Chol organizing into L_o domains surrounded by a continuous L_d phase primarily composed of EggPC. All tested NMs exert an ordering effect on this heterogeneous model. Pure CS nanoparticles show a concentration-dependent increase in GP values and induce the largest quantitative changes in lipid order. The effect of CS-based HNCs is much weaker compared to that of the pure CS nanoparticles.

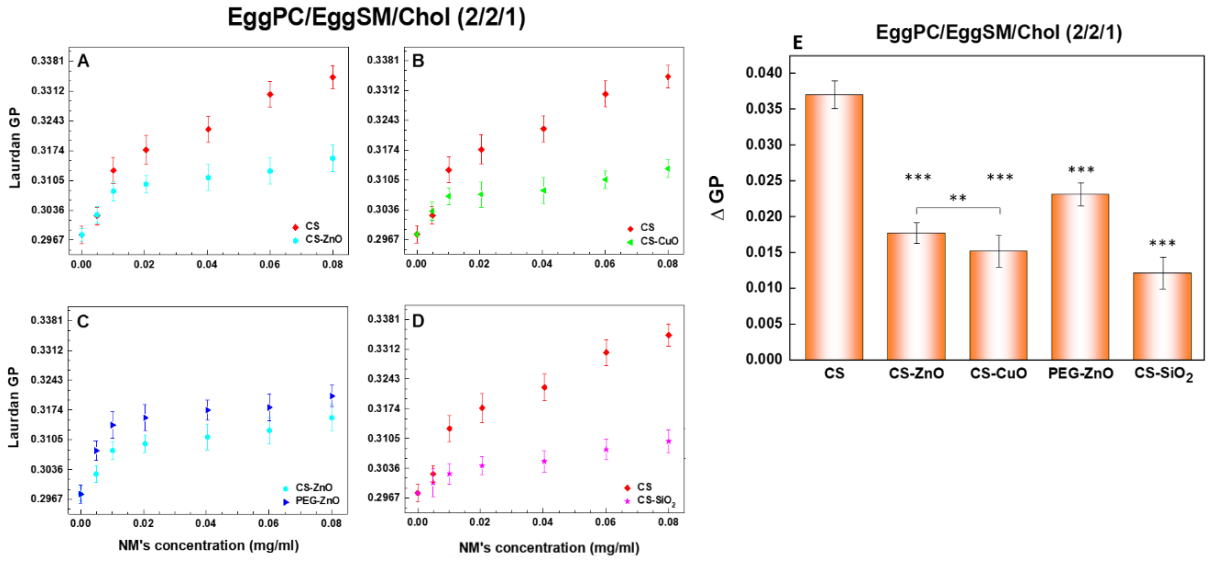

Figure 7: Laurdan GP of EggPC/EggSM/Chol LUVs as a function of NM concentration, measured at 37°C. The control GP value of EggPC/EggSM/Chol (2/2/1) is 0.2976, indicative of membranes in Ld/Lo phase coexistence. Comparison of the effects of: A) CS NPs vs. CS–ZnO; B) CS NPs vs. CS–CuO; C) PEG–ZnO vs. CS–ZnO; D) CS NPs vs. CS–SiO_2. E) Laurdan ΔGP of EggPC/Chol (1/1) LUVs as a function of NM type. ΔGP = GP (0.08 mg/mL) − GP (0 mg/mL). Statistical significance is indicated as follows: *** $p < 0.001$ (when comparing CS NPs with all types of NMs; CS–ZnO with PEG–ZnO and CS–SiO_2; CS–CuO with PEG–ZnO and CS–SiO_2; PEG–ZnO with CS–SiO_2), ** $p < 0.05$ (when comparing CS–ZnO with CS–CuO).

An interesting observation is that PEG-ZnO HNCs exhibit a stronger effect on the heterogeneous LUVs compared to the other hybrid nanomaterials (Fig. 7C and E). Such changes are not observed in the homogeneous L_d or L_o phases. The quantitative changes in lipid order in EggPC/EggSM/Chol LUVs under L_d/L_o coexistence induced by NMs follow the descending rank: CS > PEG-ZnO > CS-ZnO > CS-CuO > CS-SiO_2.

IV.2.2. Changes in Average Size, Polydispersity, and ζ-Potential of EggPC LUVs

The changes in average size, polydispersity, and ζ-potential of the model membranes induced by the NMs were evaluated using dynamic light scattering (DLS) and electrophoretic light scattering (ELS). Given that the largest changes in lipid order were observed in the L_d model upon treatment with CS NPs and CS-CuO HNCs, the colloidal properties of EggPC LUVs were investigated for these systems. The average diameter of the untreated EggPC LUVs was 110 nm, with a polydispersity ranging from 50 to 150 nm, indicating a homogeneous population of vesicles in the dispersion medium (ddH2O, pH 5.5). The DLS size of CS NPs was 38 nm, almost nine times smaller than that of CS-CuO HNCs, which had a DLS size of 334 nm. The DLS sizes of EggPC LUVs were approximately three times larger than those of CS NPs and three times smaller than those of CS-CuO HNCs. Untreated LUVs had a ζ-potential of -19 mV, indicating weak electrostatic repulsion between the vesicles in the dispersion medium. At pH 5.5, at least 40% of the amino groups of CS are expected to be protonated [3]. The interactions between the cationic CS NPs and negatively charged EggPC LUVs leads to vesicle aggregation, reflected in a concentration-dependent increase in average vesicle diameter and polydispersity. The average size of EggPC LUV/CS NP aggregates reached 312 nm with a polydispersity of 200–400 nm, as illustrated by the bars in Fig. 8A, which represent the mean width of the size distribution profile. The increase in size indicates extensive reorganization of the EggPC LUV/CS NP dispersion, with significant variation in the sizes of the formed aggregates. For CS-CuO HNCs, a similar size distribution of treated LUVs was observed, which did not depend on the tested concentrations. The tested NMs also increased the ζ-potential of EggPC LUVs. Even the lowest tested concentration (4 μg/ml) was sufficient to induce a sharp reversal of the potential from negative (-19 mV for pristine LUVs) to positive (+19 mV for NM-decorated LUVs). Increasing NMs concentration resulted in only minor changes in the absolute ζ-potential, indicating that the overall surface charge of the decorated vesicles was unaffected even at the highest concentrations. Notably, the ζ-potential values of EggPC LUVs decorated with CS-CuO HNCs were lower than those of LUVs decorated with CS NPs. This result, combined with the similar size distribution, suggests that interactions between EggPC LUVs and CS-CuO HNCs are weaker compared to those with CS NPs.

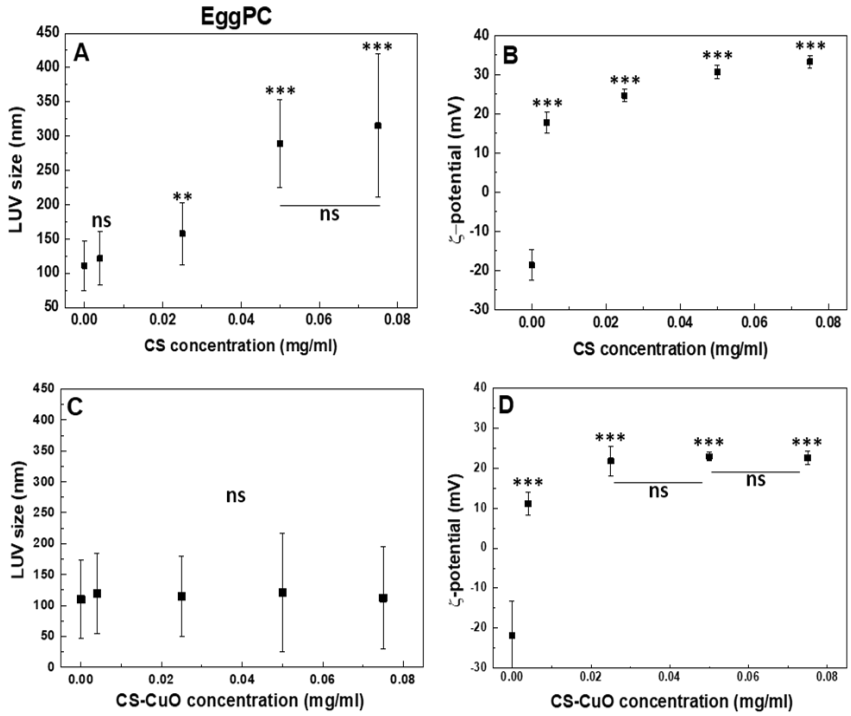

Figure 8: Effects of CS NPs (A and B) and CS–CuO HNCs (C and D) on the average size, polydispersity, and ζ-potential of EggPC LUVs. SDs were obtained from two experiments with five measurements per sample. Statistical significance is indicated as follows: *** $p < 0.001$, ** $p < 0.01$, "ns" (not significant) denotes statistically non-significant differences.

IV.2.3. Morphological Changes of GUVs Induced by Nanomaterials

IV.2.3.1. Effects on Homogeneous EggPC GUVs as an L_d Phase Model

Homogeneous giant unilamellar vesicles (GUVs) composed of EggPC were electroformed in ddH2O at pH 5.5 at room temperature (22°C). Nanomaterials were added to the observation chamber in sequential steps, with each step indicated by an asterisk in the figures. Similar to the LUV experiments, the tested NMs were added asymmetrically, interacting primarily with the outer monolayer of the bilayer membrane. Figure 9 shows the effect of pure CS NPs on homogeneous GUVs visualized by phase-contrast microscopy. During the first 15 minutes, at a CS NPs concentration of 0.02 mg/ml, no changes in vesicle volume or morphology were observed. However, after the second step, at 0.04 mg/ml, rapid adhesion between two neighboring GUVs occurred, forming a common adhesion plane (indicated by black arrows). Following the third step, at 0.08 mg/ml CS NPs, the adhered GUVs fused into a larger vesicle. This fused vesicle then progressively collapsed until it completely disappeared from the electrode surface. No visible micron-scale CS–lipid aggregates were detected in the chamber, suggesting the formation of nanoscale CS–lipid aggregates in the form of mixed micelles. The total duration of complete vesicle collapse was 289 ± 96 seconds and depended on GUV size; larger GUVs required longer collapse times. The standard deviation of collapse times was calculated from 12 vesicles across 12 independent experiments.

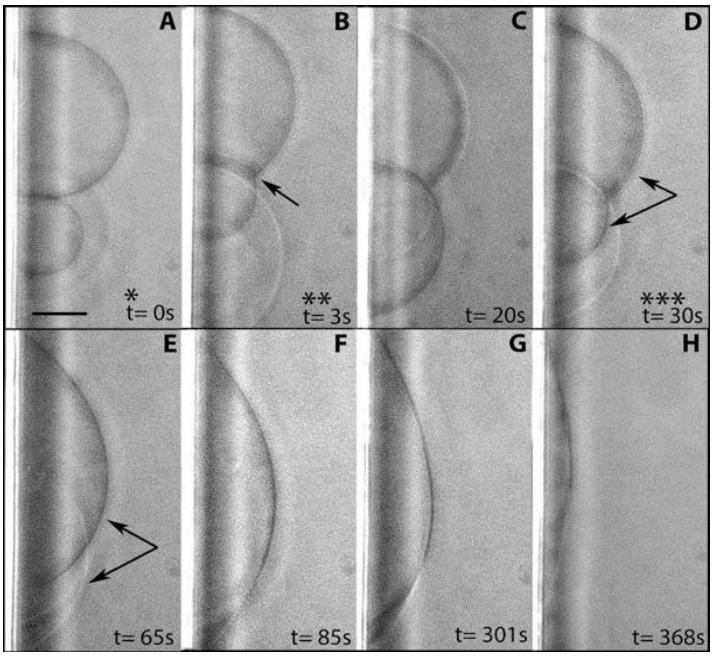

Figure 9: Effect of CS NPs on the morphology of EggPC GUVs at room temperature (22°C). EggPC GUVs were treated with aliquot concentrations of CS NPs—0.02, 0.04, and 0.08 mg/ml. A) First step: treatment with CS NPs at a concentration of 0.02 mg/ml. No changes in vesicle volume or morphology were observed (not shown in the figure). B and C) Second step: treatment with 0.04 mg/ml CS NPs at t = 0 s; rapid adhesion of two adjacent liposomes is observed, forming a flat area (see black arrows). D) Third step: at a concentration of 0.08 mg/ml CS NPs, the adhered GUVs fuse into a larger vesicle. The latter begins to gradually shrink until it disappears from the electrode surface (E–H). No micron-sized CS–lipid aggregates were observed in the working chamber. Scale bar: 20 μm.

Since CS NPs are dissolved in 1% (v/v) AA, a control experiment was conducted to assess the effect of AA on EggPC GUVs. The concentrations of NMs used in the experiments did not exceed 0.1 mg/ml, corresponding to 0.1% AA. Therefore, 0.1% AA was tested at the same concentrations used for CS NPs (Fig. 10), resulting in final chamber concentrations of 0.02 mg/ml (0.02% AA), 0.04 mg/ml (0.04% AA), and 0.08 mg/ml (0.08% AA). After the first step, at 0.04% AA, no changes in the shape of EggPC GUVs were observed (Fig. 10A and B). Five seconds after the second step, at 0.08% AA, two GUVs adhered (Fig. 10C and D, arrows). The area of the contact adhesion plane increased after the third step, at 0.16% AA (Fig. 10E). Adhesion was tracked for eight vesicles, revealing an average duration of 3.4 ± 3.7 s for adhesion to appear after the second step. Compared to CS NPs, adhesion induced by AA was stronger; however, the adhered EggPC GUVs did not undergo further morphological changes.

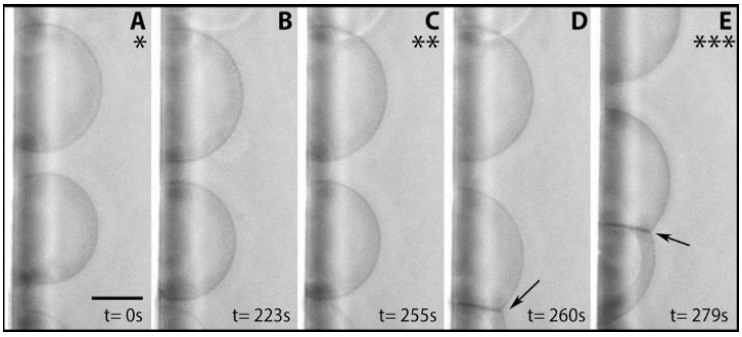

Figure 10: Effects of 0.1% AA on the morphology of EggPC GUVs at room temperature (22°C). A, B) First step: 0.02% AA, no changes in GUV morphology are observed. C and D) Second step: 0.04% AA, GUVs adhere and form a common adhesion plane (black arrows). E) Third step: 0.08% AA, the contact plane becomes larger and adhesion becomes stronger. Scale bar: 20 μm.

Treatment of EggPC GUVs with CS-ZnO HNCs produced the same morphological transformations as observed with CS NPs, but at twice the concentrations (Fig. 11). Adhesion, fusion, and progressive vesicle shrinkage were observed at 0.08 mg/m; and 0.16 mg/ml, respectively (Fig. 11D

and F). The PEG-ZnO nanocomposite induced only minor morphological changes in EggPC GUVs (Fig. 12) at the tested concentrations, with a slight reduction in vesicle volume observed at 0.04 mg/ml and 0.08 mg/ml (Fig. 12C and E).

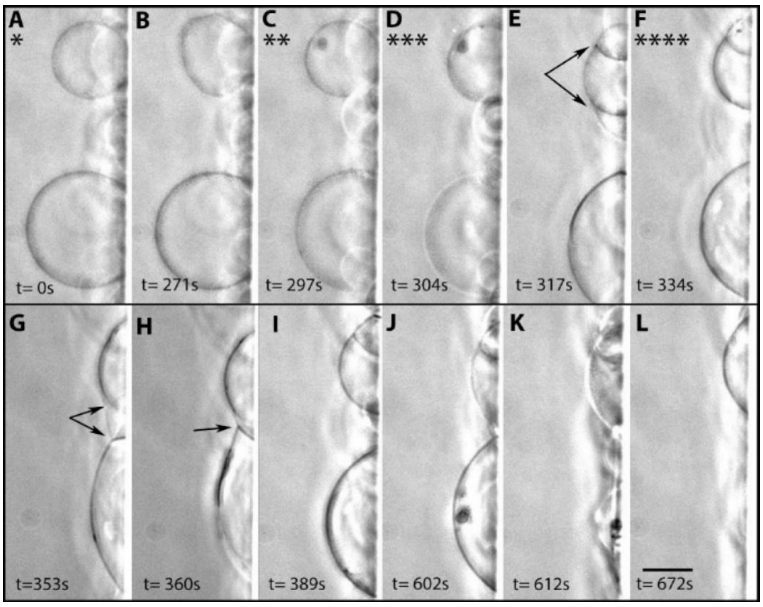

Figure 11: Effects of CS-ZnO NMs on the morphology of EggPC GUVs at room temperature (22°C). GUVs were treated with aliquot concentrations of CS-ZnO NMs: 0.02, 0.04, 0.08, and 0.16 mg/ml. A–C) First two steps, no morphological changes observed. D–E) Third step, at a concentration of 0.08 mg/ml, adhesion occurs between three GUVs with a slight reduction in their volume. F–H) Fourth step, at 0.16 mg/ml, a third adhesion is observed. I–L) Over the next 6 min, the vesicles continue to shrink until they disappear from the electrode surface. Scale bar: 20 μm.

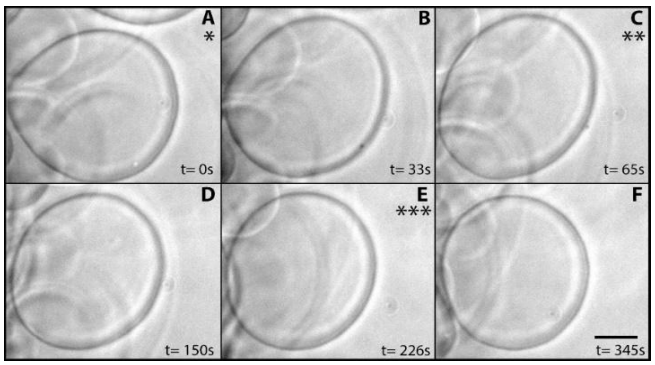

Figure 12: Effects of PEG-ZnO NMs on the morphology of EggPC GUVs at room temperature (22°C). GUVs were treated with aliquot concentrations of PEG-ZnO NMs: 0.02, 0.04, and 0.08 mg/ml. A–B) First step, treatment with 0.02 mg/mL PEG-ZnO. Slight fluctuations in the shape of the liposomes are observed. C–D) Second step, 0.04 mg/ml PEG-ZnO, slight shrinkage and rounding of the liposome. E–F) Third step, 0.08 mg/ml PEG-ZnO, minor reduction in the liposome volume. Scale bar: 20 μm.

IV.2.3.2. Effects on Heterogeneous EggPC/EggSM/Chol GUVs as an L_d/L_o Phase Coexistence Model

Eukaryotic cell membranes are heterogeneous in terms of their phase state, which is critically important for membrane structure and function. To visualize the interaction of the tested NMs with such heterogeneous membranes, GUVs composed of EggPC/EggSM/Chol (2/2/1) were used. These models exhibit L_d/L_o phase coexistence at room temperature. Phase separation in the GUVs was observed by fluorescence microscopy using unsaturated Rhodamine-PE, which preferentially partitions into the L_d phase. Consequently, the L_d phase appears as the bright, fluorescent region of the vesicle, while the L_o phase forms dark microdomains resembling raft-like domains in cell membranes (Figs. 13A, 14A). Heterogeneous GUVs were treated with CS NPs at concentrations of 0.02, 0.04, 0.08, and 0.16 mg/ml. Two types of morphological transformations were observed upon interaction with CS NPs: membrane

invaginations (Fig. 13) and shrinkage of the vesicle through the Ld phase (Fig. 14). After the first three steps, corresponding to total concentrations of 0.02 to 0.08 mg/ml CS NPs, no changes in vesicle volume or morphology were detected (Fig. 13A). At the highest tested concentration of 0.16 mg/ml, the GUV developed invaginations at three distinct locations over 2.6 min, accompanied by progressive shrinkage (Fig. 13A–H).

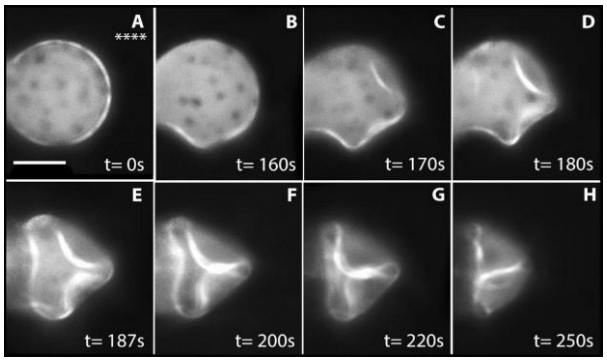

Figure 13: Membrane invaginations in heterogeneous GUVs induced by CS NPs. EggPC/EggSM/Chol (2/2/1) GUVs exhibit L_d/L_o phase coexistence at room temperature (22°C). The vesicle was labeled with 1 mol % Rhodamine-PE. GUVs were treated with concentrations of CS NPs: 0.02, 0.04, 0.08, and 0.16 mg/ml. A) Fluorescence image showing phase separation in the GUV – dark L_o domains surrounded by the fluorescent L_d phase (white areas). At CS NP concentrations from 0.02 to 0.08 mg/ml, no morphological changes were observed (data not shown). B–H) At the highest concentration of 0.16 mg/ml, internal invaginations begin to appear at three distinct sites on the GUV membrane, accompanied by gradual shrinkage. The transformations involve both membrane phases. Scale bar: 20 μm.

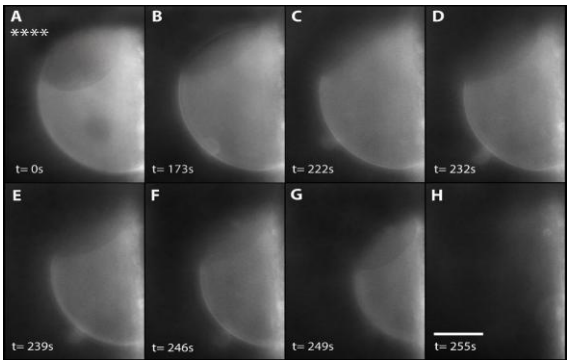

Figure 14: L_d-phase-mediated GUV shrinkage induced by CS NPs. EggPC/EggSM/Chol (2/2/1) GUVs exhibit L_d/L_o phase coexistence at room temperature (22°C). The vesicle was labeled with 1 mol % Rhodamine PE. GUVs were treated with concentrations of CS NPs: 0.02, 0.04, 0.08, and 0.16 mg/ml. A) Fluorescence image showing phase separation in the GUV – dark L_o domains surrounded by the fluorescent L_d phase (white areas). At concentrations from 0.02 to 0.08 mg/ml, no morphological changes were observed (data not shown). B–H) At 0.16 mg/ml CS NPs, progressive shrinkage of the GUV through the Ld phase is observed until it disappears from the electrode surface. Scale bar: 20 μm.

No correlation was observed between the heterogeneous membrane structure and the sites of invagination. The average rate of area reduction of the GUV was approximately 30 μm²/s. The second type of morphological transformation induced by CS NPs in heterogeneous GUVs was shrinkage through the bright L_d phase (Fig. 14). This vesicle contained one large and one smaller L_o domain at room temperature. Differences in L_o domain sizes between the two representative GUVs (Figs. 13A and 14A) reflect differences in vesicle size and membrane tension, with larger vesicles possessing larger Lo domains. The heterogeneous GUV shown in Fig. 14 was treated with the same concentrations of CS NPs, and, as in the previous experiment, a morphological effect was observed only at the highest tested concentration. Over 2.8 min at 0.16 mg/ml, the GUV progressively shrank through the Ld phase until it completely disappeared from the electrode surface (Fig. 14B–H). The average rate of vesicle area reduction was approximately 39 μm²/s. Similar to homogeneous GUVs, no visible CS–lipid micron-scale aggregates were observed in the observation chamber. These results indicate that CS NPs interact with the model membranes via disintegration of the lipid bilayer, leading to the formation of CS–lipid

aggregates smaller than a few micrometers, which is the resolution limit of optical microscopy. No micron-scale pores were observed in the GUV membrane upon interaction with CS NPs.

Control experiments on L_d/L_o GUVs using 0.1% (v/v) AA at concentrations equivalent to those used in Figs. 13 and 14 revealed that AA did not induce any morphological changes in the vesicles regardless of concentration (Fig. 15). Therefore, the activity and morphological effects of CS NPs on heterogeneous vesicles are not influenced by the AA used to dissolve the nanomaterials.

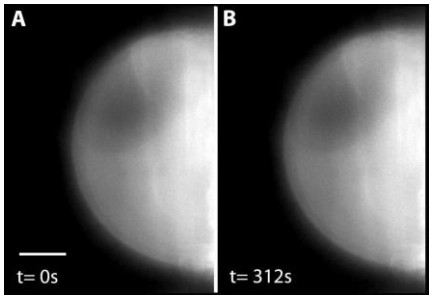

Figure 15: Effect of 0.1% AA on the morphology of GUVs composed of 2/2/1 EggPC/EggSM/Chol, exhibiting L_d/L_o phase coexistence at room temperature (22°C). Three volumetric concentrations were tested, corresponding to those used in the experiments shown in Figures 48 and 49: 0.02, 0.04, 0.08, and 0.16%. No morphological changes were observed within the investigated time frame (up to 5 min after treatment). Scale bar: 20 μm.

IV.3. Bioactivity of CS-Based HNCs Against Phytopathogenic Fungi

IV.3.1. Antifungal Activity of CS-Based HNCs

The antifungal activity of CS-based HNCs was evaluated using the agar diffusion method. HNCs were tested against fungal spore suspensions at concentrations of 50, 100, and 200 μg/well. A 0.2% DMSO solution served as the negative control, and 0.1% nystatin as the positive control (Fig. 16). The degree of antifungal activity was assessed based on the size of the inhibition zones formed around the wells, where fungal growth was absent. Antifungal activity was observed at the highest tested concentration of 200 μg/well (2 mg/ml). Both fungal strains were sensitive to the tested HNCs, with mycelial growth inhibition persisting up to 72 hours post-incubation (Fig. 16). Based on three independent cultures for each HNC–fungal strain combination, the average inhibition zones were calculated (Fig. 17). All tested HNCs exhibited a substantially stronger antifungal effect than nystatin. The highest inhibitory activity against both fungal strains was observed for CS-ZnO HNCs. Furthermore, based on the size of the average inhibition zones, *A. solani* appeared more sensitive to the tested HNCs compared to *F. solani*.

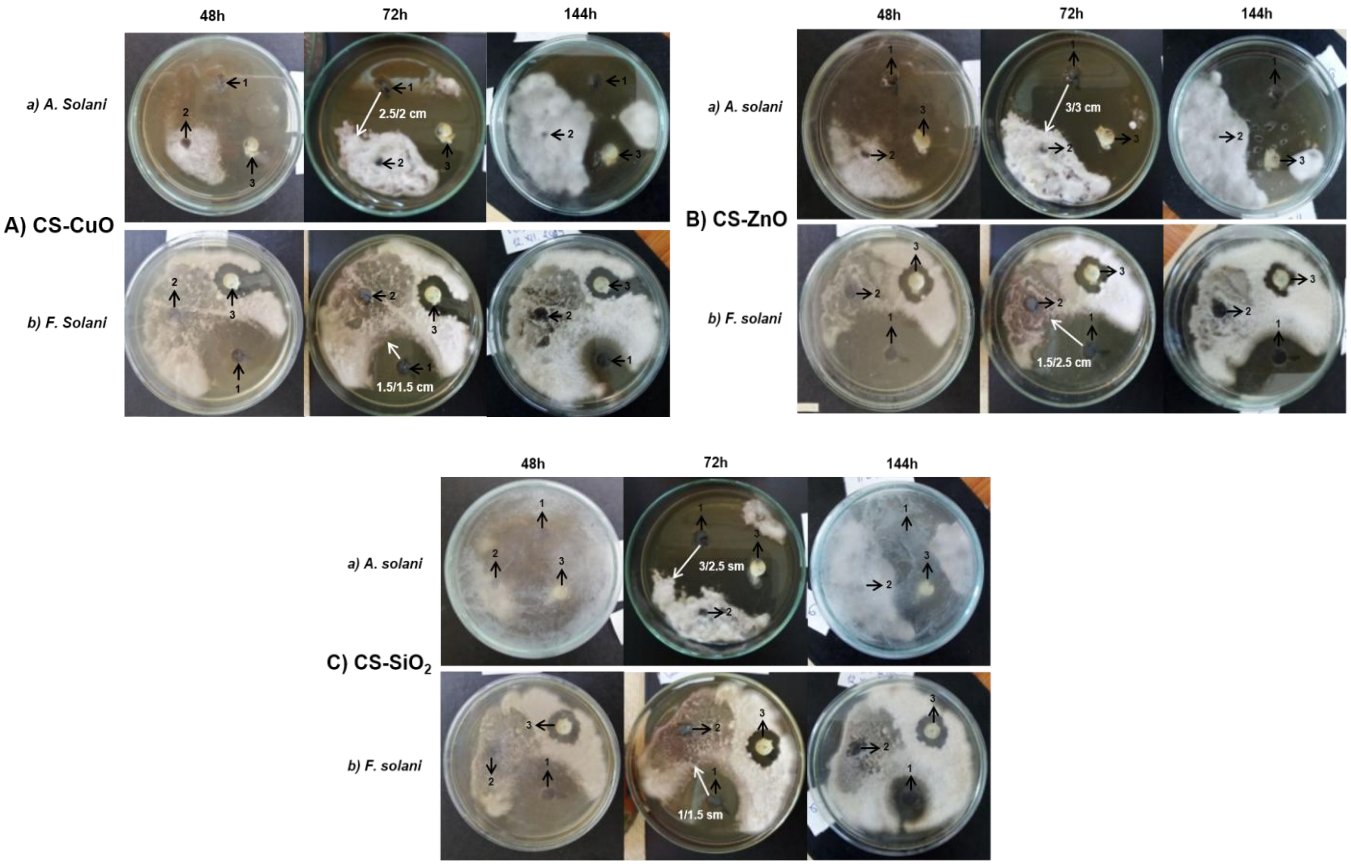

Figure 16: Antifungal activity of CS-based HNCs at a concentration of 200 µg/well, evaluated by agar well diffusion at room temperature (22°C). Effects of: A) CS-CuO HNCs, B) CS-ZnO HNCs, **C)** CS-SiO_2 HNCs on: a) *A. solani*, b) *F. solani*. Wells are labeled as: 1 – HNCs, 2 – 0.2% DMSO, 3 – 0.1%. nystatin.

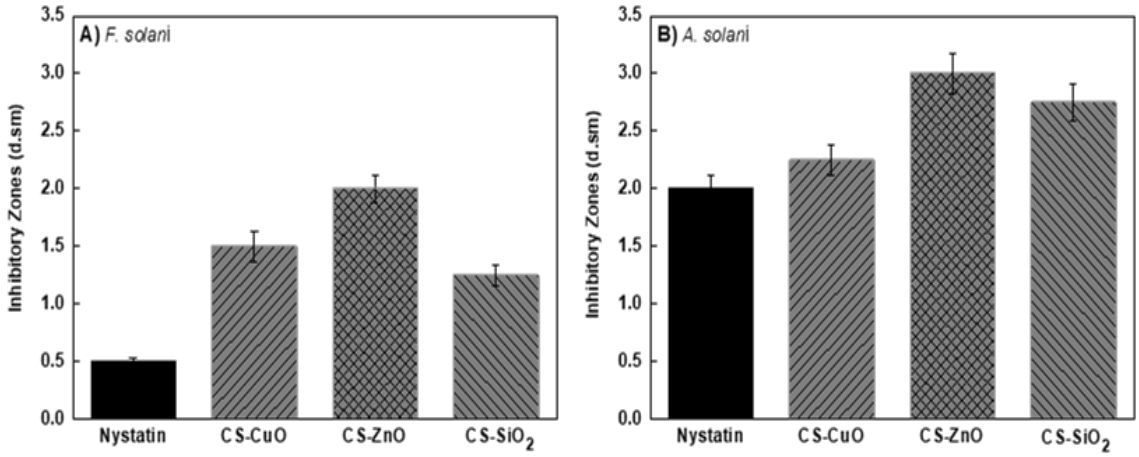

Figure 17: Average inhibition zones induced by CS-based HNCs at a concentration of 200 µg/well after 72 h incubation at 22°C. Average inhibition zones for A) *F. solani* and B) *A. solani*. The sizes of the average inhibition zones for both strains were calculated based on three replicates for each treatment type (strain × HNC type). Differences between the average inhibition zones are statistically significant – $p < 0.01$.

IV.3.2. Markers of Oxidative Stress

Fungal strains were cultured in the presence of CS-based HNCs at concentrations of 0.5 and 1.0 mg/ml. The levels of carbonyl groups are assessed as a marker of oxidatively damaged proteins, malondialdehyde (MDA) as a marker of lipid peroxidation, and super oxide dismutase SOD activity as an enzyme of the first line of cellular antioxidant defense.

In *F. solani*, elevated SOD activity was observed for all tested CS-based HNCs (Fig. 18A). The highest activity was detected upon treatment with 0.5 mg/ml CS-CuO HNCs (21 U/mg protein), more than 2.5 times higher than the control. Treatment with CS-SiO_2 and CS-ZnO HNCs led to a concentration-dependent increase in SOD activity. In *A. solani*, a significant effect was observed only for CS-SiO_2 HNCs; however, compared to *F. solani* (10–12 U/mg protein), the SOD activity was lower at both tested concentrations (6 and 8 U/mg protein) (Fig. 18B). All tested CS-based HNCs increased protein carbonyl content (PCC) in fungal cells relative to controls. A concentration-dependent effect was observed particularly for CS-CuO and CS-ZnO HNCs (Fig. 18).

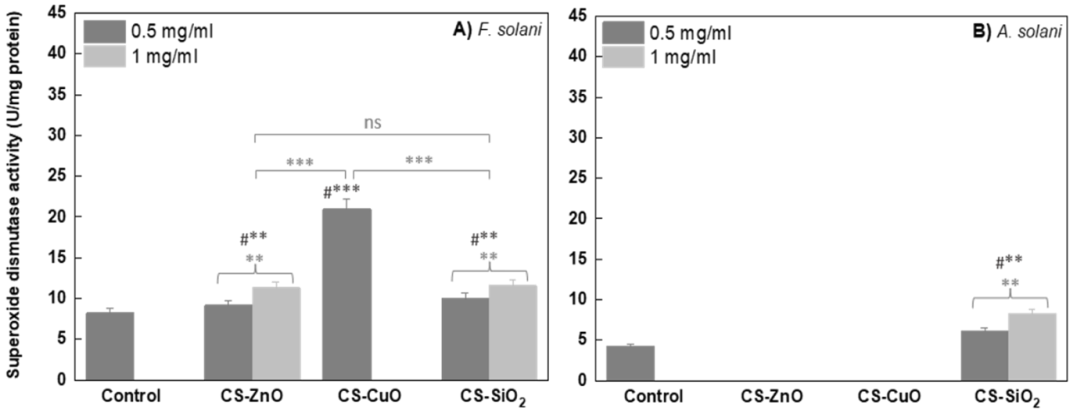

Figure 18: SOD activity levels (U/mg protein) depending on the type of HNCs at two concentrations, 0.5 and 1 mg/ml. SOD activity for: A) *F. solani* – control 8.26 U/mg protein; B) *A. solani* – control 4.25 U/mg protein. SDs were obtained from three independent experiments, each with four replicates per sample. Statistical significance among the effects of HNCs is indicated as: ***$p < 0.001$, **$p < 0.01$, *$p < 0.05$. Statistical significance between the effects of HNCs and the control is indicated as: #**$p < 0.01$, #*$p < 0.05$, "ns" denotes statistically non-significant differences.

The highest levels of protein carbonyl content (PCC) in both fungal strains were observed upon treatment with 1 mg/mв CS-CuO HNCs. *F. solani* cells exhibited higher sensitivity to 1 mg/ml CS-CuO HNCs (30 nmol/mg protein; Fig. 19A) compared to *A. solani* cells (18.45 nmol/mg protein; Fig. 19B). The lowest PCC levels were detected following treatment with CS-SiO_2 HNCs, and their effect was similar across both tested concentrations and comparable in the two fungal strains.

All CS-based HNCs induced a concentration-dependent increase in malondialdehyde (MDA) levels in fungal cells (Fig. 20). In *F. solani*, the largest effect was observed with both concentrations of CS-CuO HNCs, with MDA levels of 200 and 210 nmol/ml, nearly four times higher than the control (Fig. 20A). In *A. solani*, CS-CuO HNCs also increased MDA levels (110 and 120 nmol/ml), but to about

half the extent observed in *F. solani* (Fig. 20B). In *A. solani*, the highest effect was observed with 1 mg/ml CS-SiO_2 HNCs, resulting in MDA levels of 180 nmol/ml, 2.6 times higher than the control. The weakest effect was observed for CS-ZnO HNCs.

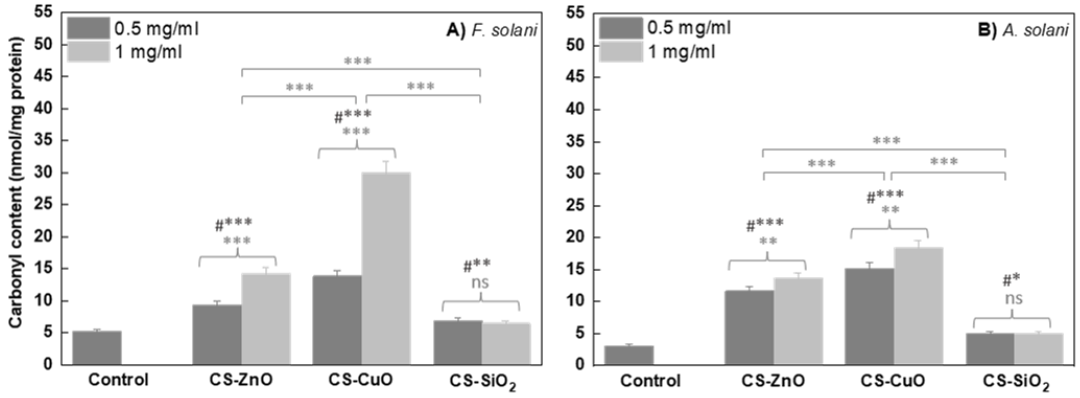

Figure 19: PCC levels (nmol/mg protein) depending on the type of HNCs at two concentrations, 0.5 mg/ml and 1 mg/ml. PCC levels for: A) *F. solani* – control 5.2 nmol/mg protein; B) *A. solani* – control 3.089 nmol/mg protein. SDs were obtained from three independent experiments, each with four replicates per sample. Statistical significance among the effects of HNCs is indicated as: ***p < 0.001 and **p < 0.01. Statistical significance between the effects of HNCs and the control is indicated as: #***p < 0.001, #**p < 0.01, #*p < 0.05, "ns" (for the comparison between 0.5 and 1 mg/ml SiO_2 HNCs).

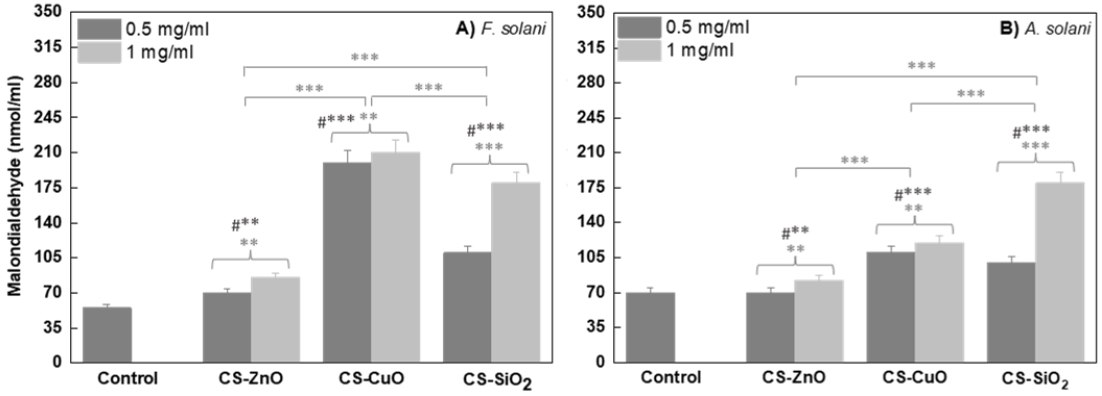

Figure 20: MDA levels (nmol/mL) depending on the type of HNCs at two concentrations, 0.5 mg/ml and 1 mg/ml. MDA levels for: A) *F. solani* – control 55 nmol/mL; B) *A. solani* – control 70 nmol/ml. SDs were obtained from three independent experiments, each with four replicates per sample. Statistical significance among the effects of HNCs is indicated as: ***p < 0.001 and **p < 0.01. Statistical significance between the effects of HNCs and the control is indicated as: #***p < 0.001 and #**p < 0.01.

IV. Changes in Lipid Order of Fungal Membranes

Quantitative changes in the molecular order of fungal membranes induced by CS-based HNCs were measured using Laurdan fluorescence spectroscopy. Both fungal strains were treated with two concentrations of HNCs, 0.5 and 1 mg/ml. The fungal suspensions and the added HNCs were incubated together for 10 minutes prior to measurement.

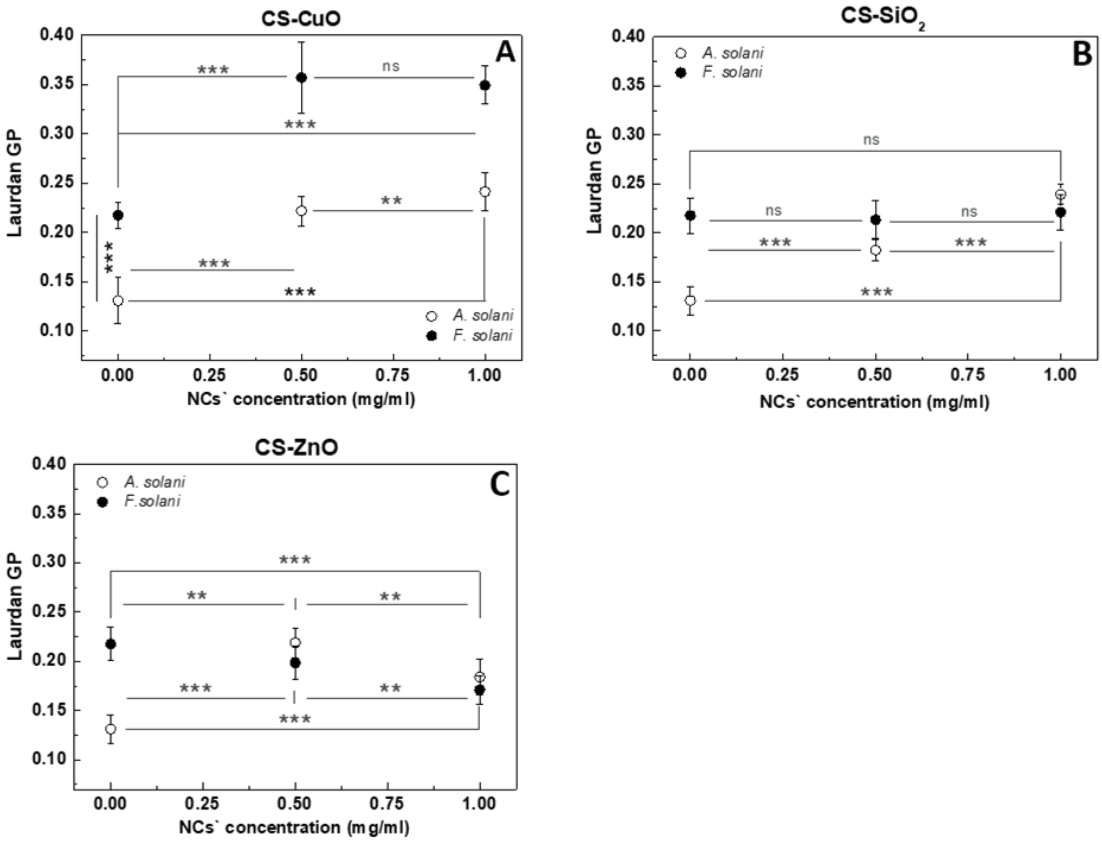

Figure 21: Laurdan GP values of membrane molecular order in ***A. solani*** and ***F. solani*** as a function of CS-based HNCs concentration, measured at room temperature (22°C). Effects of: A) CS-CuO, B) CS-SiO_2, C) CS-ZnO HNCs. SDs of GP values were obtained from three independent experiments, each with four replicates per sample. Statistical significance among GP values is indicated as: ***$p < 0.001$, **$p < 0.01$, and *$p < 0.05$. "ns" denotes statistically non-significant differences.

Elevated GP values in both fungal strains after treatment with CS-CuO HNCs indicate an increase in membrane lipid order (Fig. 21A). At the lower concentration (0.5 mg/ml), a sharp increase in GP values was observed, while at the higher concentration (1 mg/ml), no significant change in membrane order was detected. The ordering effect of CS-CuO HNCs was more pronounced in *F. solani* membranes, as reflected by the higher GP values. The CS-SiO_2 hybrid nanocomposite induced a concentration-dependent increase in membrane order only in *A. solani*, whereas in *F. solani*, these HNCs showed no significant effect at either tested concentration (Fig. 21B). A strain-dependent effect was observed for CS-ZnO HNCs (Fig. 21). In *A. solani*, treatment with CS-ZnO HNCs increased membrane order, with the strongest effect at the lower concentration of 0.5 mg/ml. In contrast, in *F. solani*, CS-ZnO HNCs caused a concentration-dependent decrease in GP values, indicative of reduced membrane order and a fluidizing effect.

Figure 22 shows the quantitative changes in fungal membrane order depending on the type of HNC tested. ΔGP represents the difference between GP values at 0.5 mg/ml and the control GP values. Among the tested CS-based HNCs, CS-CuO induced the most significant quantitative change (ΔGP =

0.1392) in the membrane order of *F. solani*. In contrast, the hybrid nanocomposites CS-ZnO (ΔGP = -0.0196) and CS-SiO_2 HNCs (ΔGP = -0.0034) (Fig. 22A) had the opposite effect, causing a reduction in membrane order, indicative of a fluidizing effect. In *A. solani*, all tested CS-based HNCs induced substantial quantitative changes, showing a pronounced ordering effect on the fungal membrane (Fig. 22B). The quantitative changes in *A. solani* induced by HNCs follow the descending order: CS-SiO_2 (ΔGP = 0.1081) > CS-CuO (ΔGP = 0.1004) > CS-ZnO (ΔGP = 0.0877).

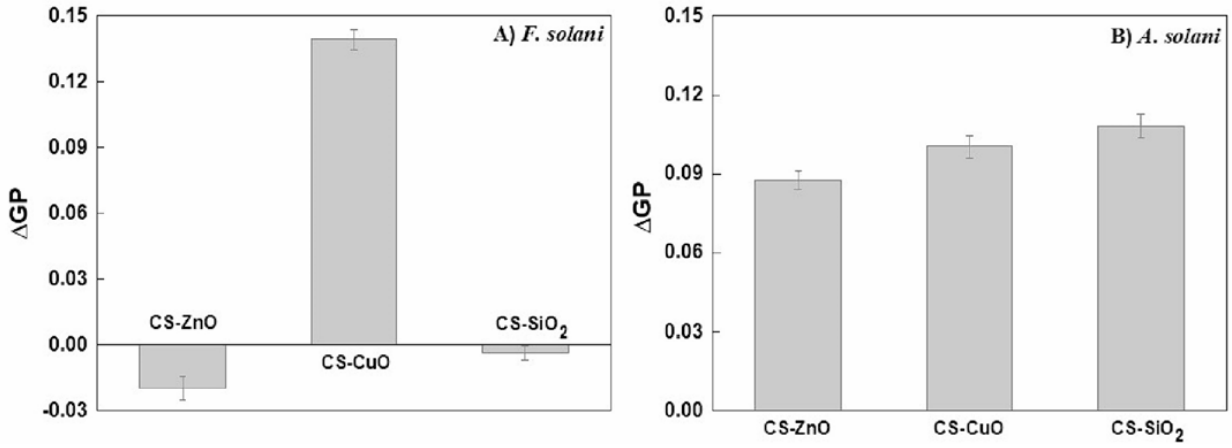

Figure 22: Laurdan ΔGP values in the two fungal strains as a function of the type of CS-based HNCs at 22°C. ΔGP = GP (0.5 mg/ml) − GP (0 mg/ml). Quantitative changes in the membranes of: A) *F. solani*; B) *A. solani*. The differences in membrane order between the two strains, induced by each type of CS-based HNCs, are statistically significant **(**$p < 0.01$).

V. Discussion

V.1. Interactions of CS-Based and PEG-Based HNCs with Membrane Models Mimicking the Phase Heterogeneity of Eukaryotic Cell Membranes

Using simplified membrane systems devoid of protein components and with clearly defined lipid phases, key principles of interaction were established, along with correlations between the observed effects and the physicochemical properties of the tested NMs. Both CS-based and PEG-based HNCs possess combinations of characteristics consistent with good bioactivity. According to the obtained HR-TEM images, all NMs exhibit a spherical shape (Fig. 1), which is considered biologically compatible and suggests enhanced cellular internalization. The DLS profiles indicate that the average sizes of the NMs range from 38 nm to 1.1 μm, while their ζ-potentials vary from +10 to +34 mV (Table 1). Despite these differences, all tested NMs demonstrate bioactivity, interact with membrane models, and induce structural and morphological changes in the bilayer across different lipid phases.

V.1.1 Effects of NMs on Lipid Order in Homogeneous and Heterogeneous Phases

Changes in lipid order in different membrane phases upon interaction with NMs were assessed by measuring the generalized polarization (GP), which reflects changes in polarity (hydration) at the level of the lipid glycerol backbone. The results indicate that all tested NMs interact with membrane lipids in various phases and alter their organization. The most pronounced effect was observed for CS NPs on the highly fluid Ld phase composed of EggPC. Pure CS NPs decreased the polarity around the glycerol backbone in a concentration-dependent manner, increasing the lipid order in this region of the bilayer. This finding aligns with previous studies showing that the ordering effect of CS NMs increases with higher polyunsaturated fatty acids (PUFAs) content in model membranes, which predominates in an L_d phase [5]. Due to their cationic charge, CS NPs (+34 mV) are electrostatically attracted to the negatively charged EggPC membranes (-19 mV). Upon adhesion to the membrane surface, CS NPs can form hydrogen bonds with the choline headgroups of EggPC [6, 7]. Hydrogen bonds are formed between free amino groups of CS (donor) and phosphate groups of EggPC (acceptor), which restricts the accessibility of water dipoles around the glycerol backbone. The reduced number and mobility of these dipoles slow Laurdan dipolar relaxation, resulting in higher GP values. Additionally, the presence of CS NPs near the glycerol region may increase the microviscosity surrounding the lipid headgroups, further contributing to delayed dipolar relaxation. Beyond electrostatic and hydrogen-bonding interactions, CS can also interact with membranes via hydrophobic interactions [6, 7]. The small size of CS NPs (~40 nm) allows partial penetration into the bilayer, enabling interactions with its hydrophobic core [6]. This can physically displace water molecules near the lipids, reducing membrane polarity and increasing lipid order at this depth.

CS-based HNCs containing ZnO, CuO, and SiO_2 induced smaller quantitative changes in Ld phase lipid order. Their lower ζ-potentials result in approximately twofold weaker electrostatic interactions with membranes compared to CS NPs. Their larger particle sizes further reduce the surface-

to-volume ratio, decreasing the number of membrane interactions [8]. Consequently, these HNCs do not penetrate deeply into the bilayer and primarily interact at the membrane surface at the tested concentrations. The PEG-ZnO hybrid nanocomposite induced the smallest changes in Ld phase order. DLS measurements show this HNC has the largest size (1.1 μm) and the lowest ζ-potential (+10 mV), approaching near-neutrality [9]. This combination of size and charge impedes efficient membrane interactions. Nevertheless, the weak ordering effect may be attributed to PEG's high hydrophilicity, which allows partial dehydration of PC membranes and reduces bilayer polarity [10].

In membrane systems containing Chol, the quantitative changes induced by NMs were significantly lower than in the L_d phase. Two types of binary mixtures—EggPC/Chol and EggSM/Chol (1/1)—were used as models of ordered Lo phases. The ordering effect on the EggPC/Chol L_o phase was three times greater than that observed in the raft-like EggSM/Chol L_o phase. The presence of Chol reduces NM adhesion to the membrane surface [11]. On one hand, Chol lowers the surface charge density, weakening interactions with cationic NMs [12]. On the other hand, Chol condenses the bilayer, creating L_o membranes with intrinsically high lipid order, which cannot be further increased by NMs. Therefore, the more disordered and polar a bilayer is initially, the stronger the ordering effect of the tested CS-based NMs.

A ternary mixture of EggPC/EggSM/Chol (2/2/1) exhibits L_d/L_o phase coexistence at physiological temperature (37 °C). This mixture was therefore selected as the most suitable model for the phase heterogeneity of eukaryotic plasma membranes. Quantitative changes in lipid order in these heterogeneous systems were larger in the L_d phase and smaller in the L_o phase, with the strongest effect observed for CS NPs. These results suggest that cationic CS NPs preferentially interact with the fluid L_d phase in heterogeneous membranes. The L_d phase is more polar, contains low levels of Chol, and has a more negatively charged surface. L_o phases are tightly packed, less polar, and possess a reduced negative surface charge due to high Chol content, resulting in weaker interactions with NMs.

V.1.2. Changes in Colloidal Properties of Membrane Models

Changes in the colloidal properties of EggPC LUVs upon interaction with CS NPs and CS-CuO HNCs were assessed by DLS and ELS. The ζ-potential of untreated EggPC LUVs is –19 mV (Fig. 45), indicating a negatively charged surface. The polar headgroup of EggPC is zwitterionic, and its protonation/deprotonation state depends directly on the pH of the medium. At pH > 4, the choline headgroup becomes negatively charged [13] due to deprotonation of the phosphate moiety and the attraction of counterions from the quaternary amine. EggPC LUVs were dispersed in ddH_2O at pH 5.5, contributing to the negative ζ-potential in this medium. Dispersions of CS NPs were also prepared in ddH_2O at pH 5.5, and the ζ-potential of CS NPs under these conditions is +33.5 mV, resulting from protonation of free amino groups. CS is positively charged in acidic solutions at pH < 6.3 [3].

The difference between the cationic NMs and the negatively charged EggPC LUVs generates electrostatic attraction, leading to adhesion of NMs to the membrane surface. This is reflected in the

sharp shift of ζ-potential from negative (–19 mV) to positive (+19 mV). As the concentration of CS NPs increases, the ζ-potential of the decorated vesicles rises, indicative of CS NP adhesion to the membrane surface. This decoration gradually reduces electrostatic repulsion between vesicles and induces their aggregation in the dispersion. DLS profiles of the CS NP/EggPC LUV dispersion show that the average size of the resulting aggregates (312 nm) is three times larger than the control (110 nm), with significantly increased polydispersity (200–400 nm), indicating a heterogeneous population of aggregates. Similar results have been reported for saturated phosphatidylcholine model systems, where CS NPs increased the ζ-potential, mean size, and polydispersity of DPPC (dipalmitoyl phosphatidylcholine) vesicles [6]. CS-CuO HNCs have a relatively lower ζ-potential (+16 mV) compared to CS NPs, due to interactions between the metal oxides and polymer during synthesis. These interactions lead to agglomeration and formation of larger HNCs (~438 nm). Nevertheless, sufficient amino groups remain exposed on the HNC surface, maintaining their cationic charge at pH 5.5 (ddH_2O). Despite their significantly larger size, CS-CuO HNCs induce similar changes in vesicle ζ-potential but do not alter their mean size or polydispersity. This suggests that the colloidal interactions with the membrane models proceed via a different mechanism, influenced by the lower charge and larger size of the HNCs.

DLS studies by other authors have shown that colloidal interactions between solid NMs and phosphatidylcholine membrane models are influenced by particle concentration and size [14, 15]. Increasing the concentration or the mean size of NPs results in a shift of the peak in the DLS profile of NP/LUV dispersions toward that of the pure NPs. At low NP concentrations, when the lipid-to-NP ratio is higher, the DLS profile may show either a single peak close to that of the pure LUVs or two peaks—one corresponding to the interacting population (NPs/LUVs) and another for non-interacting LUVs [15]. This phenomenon occurs in the intermediate zone between the distribution profiles of pure LUVs and pure NPs. At high NP concentrations, the pure LUV population may interact with the NPs, leading to a single peak in the DLS profile of the dispersion, coinciding with that of the pure NPs. Similar colloidal interactions are observed with increasing NP size. Small NPs (5–10 nm) form a dispersion with a DLS profile matching pure LUVs, medium-sized NPs (25–35 nm) show a bimodal distribution positioned between pure LUVs and pure NPs, while large NPs (50–60 nm) produce a DLS profile that coincides with pure NPs [14]. These observations indicate that when LUVs are treated with solid NPs, which act as a matter donor, the DLS profile of the treated models shifts toward that of the pure NPs.

For the CS NPs/EggPC LUVs dispersion at the lowest CS NP concentration (4 μg/mL), the DLS profile was identical to that of pure LUVs (distribution peak at 110 nm) and was far from the distribution peak of CS NPs, centered at 38 nm. With increasing CS NP concentration, a single distribution peak was observed, shifted toward larger sizes with increased distribution width. This indicates aggregate formation and increased polydispersity in the CS NPs/EggPC LUV dispersion. In contrast, for CS-CuO HNCs, the DLS profile of CS-CuO HNCs/EggPC LUVs showed, regardless of concentration, a size

distribution matching that of pure LUVs, without any shift. In the DLS profiles of both types of dispersions (CS NPs/EggPC LUVs and CS-CuO HNCs/EggPC LUVs), no new peaks corresponding to the size distribution of pure NPs were observed. This indicates that all added NMs interacted with the vesicles. Despite the significant differences in size and ζ-potential, both types of NMs decorated the vesicles, and material exchange processes occurred between them. The larger size and lower ζ-potential of CS-CuO HNCs result in different colloidal behavior, likely due to weaker and fewer interactions with the membranes. This is supported by other studies showing that smaller particles have a higher probability of cooperative adsorption on the membrane surface and penetration into the bilayer. Conversely, increasing particle size leads to reduced interactions and the occurrence of several separate adsorption events on the membrane [14].

V.1.3. Morphological Changes in Homogeneous and Heterogeneous Membranes

The effect of NMs on membrane morphology was assessed using GUVs in L_d phase and L_d/L_o phase coexistence. The results showed that the tested NMs interact with the membranes in a way that induces distinct morphological changes. Previous studies examining the effects of cationic NMs on GUV morphology composed of varying ratios of zwitterionic and anionic lipids have shown that NMs can induce a series of specific transformations, including adhesion, fusion, shrinkage, pore and tubule formation, as well as membrane permeabilization [16]. Electrostatic attraction plays a key role in determining the binding strength between cationic NMs and negatively charged GUVs [16]. When the binding energy is low due to weak electrostatic interactions, cationic NMs induce only adhesion between vesicles. In contrast, strong electrostatic forces result in high binding energy, leading to fusion and shrinkage of vesicles up to their complete disintegration [16].

In the present study, similar NM-induced morphological transformations of GUVs were observed. Increasing the volumetric concentration of NMs in the working chamber modulated the overall electrostatic attraction and the binding strength between NMs and GUVs. On EggPC GUVs, the strongest effect was observed with CS NPs, due to their highest positive charge and smallest size. At the lowest concentration of 40 μg/ml, NPs induced adhesion between adjacent GUVs. Membrane integrity disruption and increased permeability were observed at the highest volumetric concentration of CS NPs (80 μg/ml). CS-ZnO HNCs induced the same sequence of morphological changes but at twice the concentrations—fusion at 80 μg/ml and shrinkage at 160 μg/ml. The higher concentration threshold for these HNCs is attributed to their lower ζ-potential and larger size, resulting in weaker interactions with GUVs. PEG-ZnO HNCs exhibited the weakest effect, due to their near-neutral charge and largest average size among all tested NMs. A clear correlation was observed between the results obtained on GUVs and those from Laurdan fluorescence spectroscopy. As previously cited, the effects of NMs on lipid ordering in EggPC LUVs follow the descending rank: CS NPs > CS-ZnO ≈ CS-CuO HNCs > PEG-ZnO HNCs. Accordingly, it is evident that the larger the quantitative changes in membrane lipid order, the lower the NM concentration required to induce morphological transformations such as adhesion,

fusion, and shrinkage of vesicles. Compared to CS-ZnO HNCs and PEG-ZnO HNCs, CS NPs induce the largest changes in lipid order and simultaneously have the lowest concentration threshold (40 μg/ml) for inducing morphological changes. The cationic CS NPs strongly attract the negatively charged surface of EggPC GUVs. They adhere to the membrane surface, spreading across the outer membrane until full coverage of the vesicle surface is achieved, reaching a so-called stationary state. The gradual decoration of the membrane with CS NPs reduces the electrostatic repulsion between neighboring GUVs, leading to their subsequent adhesion. Above the concentration threshold of 80 μg/ml, adhesion disappears, and vesicles fuse into a larger one, which progressively shrinks until it completely vanishes from the electrode surface. The disrupted membrane permeability results from continuous ordering of the lipid bilayer by the presence of NPs. At the highest concentrations, CS NPs can penetrate deeply into the membrane, creating local deformations and transient pores, causing the observed vesicle shrinkage and the release of submicron lipid-NP aggregates.

In the experimental GUV models, adhesion, fusion, shrinkage, and complete vesicle disintegration were observed at specific CS NP concentrations. This phenomenon is partially corroborated by LUV experiments, in which the size distribution profile of LUVs increased over the tested CS NP concentration range. In the DLS profile of treated LUVs, no distribution peak shifted toward smaller sizes relative to untreated LUVs, which could correspond to the formation of small vesicles or micelles (vesicle disintegration). Differences in size, surface tension, and curvature between GUVs and LUVs are critical factors that can influence NM-membrane interactions, including binding affinity, penetration, lipid bilayer destabilization, and other effects.

CS NPs induce morphological changes in heterogeneous GUVs (EggPC/EggSM/Chol), which display L_d/L_o phase coexistence, but at twice the concentration (160 μg/ml). Two types of morphological transformations were observed in the heterogeneous GUVs—internal membrane invaginations and gradual shrinkage of GUVs through the L_d phase. As discussed in the LUV results, the cholesterol content affects the membrane's interaction with cationic NMs. Cholesterol reduces the negative surface charge of the membrane, thereby decreasing electrostatic interactions with cationic NPs. CS NPs interact primarily with the L_d phase by increasing its lipid order. Above a critical concentration of CS NPs—in this case, 160 μg/ml—the uneven distribution of NPs across the membrane surface and their differential effects on the lipid ordering of the two coexisting phases trigger the observed inward membrane invaginations and membrane disintegration.

V.2. Biological Activity of CS-based HNCs Against Phytopathogenic Fungi

V.2.1. Antifungal Activity of CS-based HNCs Against *A. solani* and *F. solani*

The newly synthesized CS-based HNCs are composed of highly effective components with pronounced antifungal activities. Numerous studies have reported the antifungal effects of various CS NMs against phytopathogenic fungi such as *Rhizopus* sp. [17], *Colletotrichum capsica* [18], *Fusarium*

graminearum, and *Botrytis cinerea* [19]. The strength of this activity depends on the degree of deacetylation (DD) and molecular weight (MW) of CS, as these factors determine the size of the NMs and the magnitude of the cationic charge [17, 20]. In addition to CS, metal oxides such as ZnO and CuO have also demonstrated remarkable antifungal activity against key pathogens, including *Botrytis cinerea* [21], *Penicillium expansum* [22], and *Fusarium oxysporum* [23]. Furthermore, recent studies have highlighted the strong inhibitory effects of SiO_2 NPs against agricultural phytopathogenic fungi [24, 25].

The chemically combination of the organic CS with inorganic oxides (ZnO, CuO, and SiO_2) represents an innovative approach for creating stable and antifungal HNCs. This has been shown to be an effective strategy to enhance the activity of both CS and the inorganic oxides, resulting in a synergistic antifungal effect [26]. Another major advantage of these HNCs is the demonstrated biocompatibility of both components, as they do not pose undesired risks to plants or the environment. CS is particularly valuable due to its biodegradability and proven plant growth-promoting activities [27]. Likewise, CuO and ZnO are well-known in agriculture as effective fertilizers, supporting the growth and development of crops [28, 29].

Despite the presence of highly active components in CS-based HNCs, their efficacy largely depends on the combination of their physicochemical properties, such as size, shape, and surface charge. Spherical NMs exhibit a strong antifungal effect because they are internalized more rapidly and efficiently into fungal cells [4, 30]. NM size is also a critical factor influencing their activity. For example, small NMs (ranging from 40 to 100 nm) display potent antifungal effects and effectively inhibit the growth of fungal mycelia and spores [31–33]. Their small size provides a high surface-to-volume ratio, rendering their surface highly reactive and facilitating interactions with fungal cell surfaces [8, 34]. Very small NMs can also induce nanotoxicity by compromising cell membrane integrity, leading to fungal cell lysis [35].

The surface charge of NMs plays a key role in their interactions with fungal cell surfaces and critical cellular components. Studies have shown that positively charged NMs exhibit significantly stronger antifungal activity compared to negatively charged ones [36, 37]. Fungal cell walls possess a negative surface charge due to the presence of phosphorylated mannosyl residues on their surface [38]. This results in electrostatic attraction of positively charged NMs to the negatively charged fungal surfaces, promoting effective adsorption, internalization, and subsequent interactions [39].

CS-based HNCs were synthesized to achieve high antifungal activity. The resulting HNCs meet the criteria for effective antifungal performance. They are spherical in shape, with high positive ζ-potentials ranging from +22 to +30 mV, and small average sizes between 65 and 167 nm. During the HNC preparation, an additional protonation step followed by lyophilization was performed to ensure maximal protonation of the CS amino groups and their effective dispersion in DMSO. This process yields smaller colloidal sizes and higher positive charges, which may contribute to enhanced toxicity

when interacting with fungal cells. Results from the agar diffusion assay demonstrated that the tested CS-based HNCs exhibit strong antifungal effects against the phytopathogenic fungi *A. solani* and *F. solani*, even surpassing the activity of nystatin, a widely used potent fungicide. The HNCs effectively inhibited mycelial growth at a concentration of 200 µL/well, maintaining activity up to 72 h post-treatment. Between the two strains, *A. solani* was more sensitive to HNCs compared to *F. solani*. Among the tested HNCs, CS-ZnO HNCs showed the most potent antifungal effect, inducing large inhibition zones in both fungal strains.

V.2.2. Mechanism of Antifungal Activity of the CS-based HNCs

V.2.2.1. Induction of ROS and OS

Among the proposed mechanisms explaining the antifungal activity of NMs, their ability to induce high levels of oxidative stress (OS) is one of the most significant and extensively studied. Exogenously induced reactive oxygen species (ROS) cause irreversible damage to numerous cellular components, including DNA, proteins, and lipids, leading to severe disruptions in cellular homeostasis and ultimately cell death.

It has been established that, due to its polycationic nature, CS can induce high levels of ROS and subsequent cell death in various fungal species [40, 41]. As a polycation, CS in certain nano formulations may exhibit pro-oxidant activity [42] and can induce ROS formation either directly or indirectly. The precise mechanism by which CS generates ROS, however, remains unclear. Studies on *Neurospora crassa*, for example, suggest that CS-induced ROS levels are associated with membrane permeabilization. Upon CS treatment, this fungus displays an increased metabolic response to ROS through the activation of genes involved in membrane homeostasis [43]. Additionally, CS may act as a chelating agent, binding nutrients and minerals in the medium, which can lead to fungal cell starvation, metabolic disturbances, and potentially further OS generation [44].

On the other hand, metal oxides such as ZnO and CuO have well-established mechanisms for generating oxidative stress (OS) in cells. They are characterized by strong pro-oxidant activities and can produce reactive oxygen species (ROS) through various mechanisms. One such mechanism is redox-surface catalysis. The crystalline nanostructure of ZnO and CuO contributes to numerous highly reactive structural defects on their surfaces, where O_2 molecules can be reduced to superoxide anions ($O_2^{\bullet -}$) (Fig. 1) [45, 46]. These superoxide anions, in turn, can significantly increase active SOD levels and trigger the generation of other toxic ROS, such as H_2O_2 and hydroxyl radicals ($OH^{\bullet}$) [46]. Additionally, ZnO can release Zn^{2+} ions, which induce metabolic disturbances, enzyme deactivation, and disruptions in ionic homeostasis, potentially causing OS within the cells [47].

To assess the pro-oxidant activity of CS-based HNCs, in-depth cultures of *F. solani* and *A. solani* were treated with HNCs. The resulting measurements of superoxide dismutase (SOD) activity, MDA levels, and PCC content unambiguously demonstrated the presence of OS in the fungal cells. The

metalloenzyme SOD plays a central role in cellular antioxidant defense against ROS by dismutation $O_2^{\bullet-}$ into H_2O_2 and O_2 (Fig. 21) [48]. Elevated SOD levels are a strong indicator of intracellular $O_2^{\bullet-}$ presence and overall oxidative stress. In *F. solani* cells, SOD levels increased in response to all tested HNCs, with CS-CuO HNCs exhibiting the most pronounced effect even at the lowest tested concentration of 0.5 mg/ml. In contrast, in *A. solani*, SOD activity was influenced only by CS-SiO_2 HNCs. The lower SOD levels and the absence of activity in response to other HNCs in *A. solani* cells indicate rapid dismutation of $O_2^{\bullet-}$ by SOD.

In addition to activating cellular antioxidant systems, high levels of oxidative stress (OS) induce various cellular damages. The cell membrane, for example, is one of the most vulnerable components and can be targeted by ROS-induced oxidative damage. The primary and most toxic radical capable of initiating lipid peroxidation is the hydroxyl radical (OH•) [49]. A key marker for detecting LP in cells is the aldehyde malondialdehyde (MDA), as it is one of the main secondary products of oxidative damage to membrane lipids [50]. The results showed that all tested CS-based HNCs induced a clear dose-dependent increase in MDA levels in both fungal strains. The membranes of *F. solani* appeared more sensitive to CS-CuO HNCs, whereas those of *A. solani* were more responsive to CS-SiO_2 HNCs, as indicated by the levels of MDA induced.

High intracellular OH• levels also lead to the carbonylation of amino acid residues in cellular proteins through the addition of ketones or aldehydes to their native structure. This, in turn, disrupts protein structure and function, potentially causing cross-linking, fragmentation, denaturation, and proteolysis. Moreover, elevated protein carbonyl content (PCC) in cells may result from interactions with secondary aldehydes generated during LP, including MDA, which react with amino acid residues and induce their carbonylation [51, 52]. The obtained results demonstrated that PCC levels in both strains increased significantly in response to all tested HNCs. In both fungal species, the highest PCC levels were observed following treatment with CS-CuO HNCs.

The results indicate that *F. solani* is more sensitive to the pro-oxidant activity of CS-based HNCs, showing significantly elevated levels of all measured oxidative stress (OS) markers. The greatest sensitivity was observed in response to CS-CuO HNCs. CuO is highly toxic to fungal cells. Its activity, in addition to redox-surface catalysis, is based on the release of Cu^+ and Cu^{2+} ions, which participate in Fenton-like and Haber–Weiss reactions, leading to high intracellular OH• levels (Fig. 2) [45, 47, 53]. These highly toxic radicals oxidize proteins and membrane lipids [114], correlating with the increased MDA and PCC levels. Moreover, the reduced Cu^+ and oxidized Cu^{2+} forms can engage in redox cycling with lipid hydroperoxides (LOOH) during lipid peroxidation, amplifying the peroxidation process and causing further membrane damage (Fig. 32 (5,6)) [50].

In *A. solani*, the strongest effect was observed with CS-SiO_2 HNCs, resulting in the highest levels of active SOD and MDA. This pronounced pro-oxidant activity of SiO_2 is likely attributed to the nano structural organization of SiO_2 within the HNCs. Although SiO_2 is amorphous and inert, decreasing

particle size imparts pro-oxidant properties. It has been shown that the smaller the NPs, the greater the likelihood of ROS formation and OS induction in cells [8]. This is due to the increased number of highly reactive structural defects on the particle surface, which alter the oxide's redox potential to biologically relevant values. Consequently, the SiO_2 NP surface becomes more reactive and capable of participating in redox-surface catalysis [45]. Although slower than Fenton and Haber–Weiss reactions, this catalysis results in prolonged oxygen reduction and elevated ROS levels within the cells.

It is important to note that, despite the strongly pro-oxidant oxides in these HNCs, surface charge is a key factor contributing to oxidative stress (OS) in fungal cells. All CS-based HNCs are cationic, with high ζ-potentials ranging from +22 to +30 mV. It has been demonstrated that cationic NMs induce very high ROS levels due to electrostatic interactions with cellular components, which alter their redox potential and disrupt their functions [54].

V. Lipid Organization Alternations in the Fungal Membranes

Changes in the lipid order of fungal membranes following treatment with CS-based HNCs were assessed by calculating the general polarization (GP), similar to studies conducted with LUVs. Investigating these changes is a key aspect of the HNCs' mechanism of action, as the membrane represents the primary target of their effects. Alterations in membrane lipid order led to disruptions in permeability and integrity, which are directly associated with the nano toxic activity of the materials.

The results show that the observed antifungal activity of the studied CS-based NCs is accompanied by changes in the lipid order of fungal membranes in both strains. Control GP values of the fungal membranes were high and positive (*F. solani* – GP = 0.224; *A. solani* – GP = 0.126), indicating that the fungal membranes are ordered under normal conditions. Fungal cell membranes are composed of ergosterol, sphingolipids, and glycerophospholipids [55], and their specific fatty acid composition confers a defined degree of order under physiological conditions. Following treatment with CS-based HNCs, significant alterations in membrane organization were observed, with a pronounced tendency toward increased lipid order. The most pronounced quantitative changes in the membranes of *F. solani* were induced by CS-CuO HNCs, whereas in *A. solani*, the strongest effects were observed with CS-SiO_2 HNCs.

The mechanisms of action of CS-based HNCs on membrane models can be applied to interpret the observed effects on fungal membranes. The increased lipid order in model membranes has been attributed to electrostatic interactions, adhesion to the membrane surface, reduced polarity around the glycerol backbone, and potential hydrophobic interactions with the bilayer. The physicochemical properties of the antifungal CS-based HNCs (sizes 65–167 nm and ζ-potentials of +22 to +30 mV) favor such interactions with fungal cell membranes, leading to increased lipid ordering. Although these mechanisms were derived from experiments using simplified membrane models, a correlation between effects observed in model membranes and fungal membranes can be established. This correlation demonstrates a clear trend of increased lipid order in membranes upon interaction with these cationic

HNCs. In turn, this validates the significance of membrane models as reliable systems for evaluating the bioactivity of different types of NMs. Despite the absence of protein components, these models are valuable for identifying interaction trends and highlight the key role of the lipid component in the membrane when exposed to exogenous molecules, including NMs.

The results related to changes in lipid order clearly indicate that HNCs establish direct contact with fungal membranes. One of the defining features of fungal cells is the presence of a cell wall. Nevertheless, it evidently does not prevent the penetration of HNCs and their contact with the plasma membrane. The negative charge of the cell wall may promote electrostatic attraction with cationic NMs [164]. Studies have shown that CS can traverse the fungal cell wall and interact with negatively charged phospholipids in the membrane [56, 57]. This process may also be accompanied by disruption of cell wall integrity. Supporting this, research on *S. cerevisiae* demonstrates increased expression of genes related to cell wall regulation in response to CS treatment [58], which in turn contributes to the antifungal activity of CS NMs.

The ability of antifungal agents to traverse the fungal cell wall and plasma membrane is a key factor determining their efficacy. Resistance among pathogenic fungi is mediated by various mechanisms, including alterations at the target site, detoxification or inactivation of the active compound, overexpression of target proteins, and active efflux via transport pumps [59]. Adaptive changes in cell wall composition and membrane bilayer organization also play a critical role, as they can limit the penetration and intracellular accumulation of antifungal agents. For example, increased chitin and glucan content in resistant strains leads to cell wall thickening, impeding access of external agents to the plasma membrane [60, 61]. Similarly, modifications in membrane lipid composition, including variations in ergosterol content, influence membrane order, fluidity, and permeability, thereby modulating interactions with antifungal compounds and nanomaterials [62]. In this context, the observed interactions between the investigated CS-based HNCs and fungal membranes, along with the accompanying changes in lipid order, indicate that antifungal activity is mediated via a mechanism involving direct effects on membrane organization. This represents an alternative strategy to overcome resistance in phytopathogenic fungi.

VI. Summary

Using membrane models that recapitulate the heterogeneity of eukaryotic membranes, key biophysical and physicochemical principles governing the interactions of CS-based and PEG-based HNCs with bio membranes were elucidated. The results demonstrated that newly synthesized CS NPs, CS-based HNCs containing CuO, ZnO, and SiO_2, and PEG-ZnO HNCs interact with various membrane lipids and distinct lipid phases, inducing changes in lipid organization accompanied by morphological alterations in the membranes. Electrostatic attraction plays a central role in the interactions between cationic NMs and membranes composed of zwitterionic lipids with a mildly electronegative surface charge. These interactions facilitate multiple mechanisms, including adsorption of NMs onto the membrane surface, hydrogen bonding with the polar lipid headgroups, hydrophobic interactions, and even bilayer penetration. As a result, NMs increase the order of lipid phases by reducing polarity around the glycerol backbone of the lipids. The most pronounced quantitative changes were observed in the highly fluid and polar L_d phase, followed by the L_d/L_o phase coexistence, whereas the highly ordered raft-like Lo phase exhibited the weakest alterations. The presence of cholesterol in the membranes significantly decreases the polarity and negative surface charge of the bilayer, contributing to weaker interactions of cationic NMs with the L_d/L_o and L_o phases. It was observed that the more disordered and polar the initial lipid bilayer, the stronger the ordering effect induced by the HNCs. The increase in lipid order in homogeneous L_d and heterogeneous L_d/L_o membranes induced by NMs was accompanied by changes in bilayer permeability, membrane invaginations, and disruption of membrane integrity. A clear correlation was established between the specific interactions of NMs with membranes and their physicochemical properties, such as surface charge and particle size. The strongest interactions were observed for CS NPs (38 nm, +34 mV), whereas the weakest were recorded for PEG-ZnO HNCs (1.1 μm, +10 mV). The results indicate that smaller colloidal sizes and higher positive charges of NMs lead to more pronounced effects on membranes and require lower concentrations to achieve the observed membrane alterations.

The bioactivity of newly synthesized CS-based HNCs containing ZnO, CuO, and SiO_2 was evaluated against economically important phytopathogenic fungi, *Alternaria solani* and *Fusarium solani*. The results demonstrated that all CS-based HNCs exhibited efficient and sustained antifungal activity. The strongest inhibitory effect on mycelial growth for both strains was observed with CS-ZnO HNCs. These findings indicate that combining CS with inorganic oxides represents an innovative approach for synthesizing antifungal HNCs with synergistic activity and favorable physicochemical properties. The combination of spherical morphology, small particle size (65–167 nm), and polycationic nature (+22 to +30 mV) promotes strong interactions of CS-based HNCs with the negatively charged fungal cell surfaces, facilitating rapid and efficient internalization and inducing nano toxic effects. Using biochemical and biophysical approaches, it was established that the molecular mechanisms underlying

the antifungal action of HNCs involve the induction of oxidative stress in fungal cells and alterations in lipid organization within the fungal membranes. All CS-based HNCs exhibited strong pro-oxidant activity, reflected in elevated superoxide dismutase (SOD) levels, lipid peroxidation, and protein carbonylation. The presence of these markers indicates the generation and accumulation of irreversible oxidative damage in essential cellular components and biomolecules. *F. solani* showed higher sensitivity to CS-CuO HNCs, whereas *A. solani* was more sensitive to CS-SiO_2 HNCs. The pro-oxidant activity of the CS-based HNCs is attributed to the nano structural organization of ZnO, CuO, and SiO_2, which generate high levels of ROS through multiple mechanisms, including metal ion release, redox-surface catalysis, Fenton-like reactions, and Haber–Weiss reactions. In addition to inducing oxidative stress, the antifungal activity of the NMs is accompanied by changes in membrane order in both fungal strains. The small size and cationic surface of HNCs facilitate their passage through the negatively charged fungal cell wall and enable direct contact with the phospholipid components of the plasma membrane. The interaction of HNCs with membranes induces alterations in lipid ordering, rendering the fungal membranes more susceptible to structural and functional damage. These findings highlight the membrane-targeted nature of the antifungal activity and underscore the potential of these nanomaterials as an alternative strategy against resistant fungal strains.

This work contributes not only with applied perspectives but also provides a significant fundamental insight into the mechanisms of interaction between hybrid nanomaterials and biological membranes. Key biophysical and physicochemical relationships were elucidated, linking the surface characteristics of the nanomaterials, lipid organization, and the induction of oxidative stress, thereby expanding our understanding of membrane-mediated mechanisms underlying nanotoxicity. The results highlight the considerable potential of CS-based HNCs as a new generation of antifungal agents with a dual mechanism of action, combining membrane-disrupting and pro-oxidant effects. These materials may serve as alternatives or complements to conventional antifungal agents in plant protection for the control of phytopathogenic fungi. Furthermore, they hold promise for the development of functional coatings, biocompatible nanomaterials, and antimicrobial systems aimed at overcoming increasing resistance and reducing the required active concentrations.

VII. Conclusions

1. The synthesized CS NPs, CS-based HNCs with CuO, ZnO and SiO_2 and PEG-ZnO HNCs interact with different membrane lipids and lipid phase, inducing specific alternations in the membrane models.

2. The electrostatic attractive forces between the cationic NMs and the membranes composed of zwitterionic lipids with an electronegative surface charge promote various key interaction mechanisms, including NM adhesion to the membrane surface, formation of hydrogen bonds with the polar lipid heads, hydrophobic interactions, and penetration into the lipid bilayer.

3. The tested NMs increase the order of all lipid phases, reducing polarity in the region of the lipid glycerol backbone, with this effect depending on the initial lipid order and bilayer polarity.

4. The most pronounced quantitative changes are observed in the highly fluid and polar L_d phase, while the least changes occur in the highly ordered raft-like L_o phase. The presence of Chol in the membranes reduces bilayer polarity and negative surface charge, promoting weaker interactions with cationic NMs.

5. The increased lipid order in homogeneous L_d and heterogeneous L_d/L_o membranes induced by NMs is accompanied by changes in bilayer permeability, membrane invaginations, and membrane disintegration.

6. There is a clear correlation between the observed effects on membranes and the physicochemical properties of the NMs. The strongest interactions are observed for CS NPs (38 nm, +34 mV), while the weakest are for PEG-ZnO HNCs (1.1 μm, +10 mV). The smaller the colloidal size of the NMs and the more positively charged they are, the more pronounced the observed membrane alterations, requiring lower concentrations to achieve these effects.

7. CS-based HNCs demonstrate effective and prolonged (up to 72 h) antifungal activity against the phytopathogenic fungi *Alternaria solani* and *Fusarium solani*. The strongest inhibitory effect on mycelial growth of both strains is observed with CS-ZnO HNCs.

8. The combination of CS with inorganic oxides represents an innovative approach for the synthesis of HNCs with synergistic antifungal activities and optimized physicochemical properties, including spherical morphology, small size (65–167 nm), and a polycationic surface (+22 – +30 mV).

9. The antifungal activity of CS-based HNCs is mediated through the induction of oxidative stress in the cells of the tested phytopathogens. The evaluated CS-based HNCs exhibit strong pro-oxidant activity, reflected by increased levels of SOD, lipid peroxidation, and protein carbonylation.

10. The interaction between HNCs and membranes induces changes in lipid organization, highlighting the membrane-targeted nature of their antifungal activity and the potential of these NMs as an alternative strategy against resistant fungal strains.

VIII. Contributions

The scientific contributions of this dissertation can be formulated as contributions of **fundamental (1–4)** and **applied scientific nature (5, 6):**

1. A molecular mechanism of interaction was proposed, encompassing systematic biophysical and physicochemical principles governing the interactions between cationic CS-based and PEG-based HNCs and various membrane lipids and lipid phases in model eukaryotic membranes.
2. A comprehensive biophysical and physicochemical analysis of CS- and PEG-based HNCs was performed, identifying critical parameters (size, surface charge, and morphology) that determine their interactions with model and biological membranes.
3. For the first time, the zeta potential and membrane organization in homogeneous and heterogeneous model membranes treated with CS- and PEG-based nanocomposites were quantitatively characterized, and the induced morphological transformations were visualized.
4. For the first time, it was demonstrated that the antifungal activity of CS-based HNCs against *Alternaria solani* and *Fusarium solani* is realized through a combined mechanism involving the induction of oxidative stress and substantial alterations in the lipid organization of fungal membranes.
5. A correlation was established between the physicochemical characteristics of the nanomaterials, their antifungal activity, and the induced membrane and oxidative damage in fungal cells of *Alternaria solani* and *Fusarium solani*, enabling prediction and targeted optimization of their antifungal efficacy.
6. A scientific foundation was laid for the future application of CS-based hybrid nanocomposites as effective and environmentally oriented antifungal materials for the control of *Alternaria solani* and *Fusarium solani* in agriculture, with potential use in plant protection and the development of sustainable nano biopesticides against resistant strains.

Scientific Publications

One Publication as a First Author

1. **Benkova, D**., Dishliyska, V., Staleva, J. M., Kostadinova, A., Staneva, G., El-Sayed, Kh., Elshoky, H. A., Krumova, E. (2024). CS and ZnO Nanoparticles as Fungicides Against Fungal Pathogens *Alternaria solani* and *Fusarium solani*. Mechanism Underlining Their Antifungal Activity. *Comptes rendus de lAcademie bulgare des Sciences*, 77(7), Marin Drinov, BAS, 986-996, (Scopus):0.16, JCR-IF (Web of Science): 0.3, Q3 (Scopus). http://dx.doi.org/10.7546/CRABS.2024.07.05

Two Publications as with Shared First Authorship:

2. Kostadinova, A., **Benkova, D.**, Staneva, G.., Hazarosova, R., Vitkova, V., Yordanova, V., Momchilova, A., Angelova, M. I., ElZorkany, H. E., El-Sayed, Kh., Elshoky, H. A. (2024). Chitosan hybrid nanomaterials: A study on interaction with biomimetic membranes. *International Journal of Biological Macromolecules*, 276, Elsevier, 133983. SJR (Scopus):1.245, JCR-IF (Web of Science):7.7, Q1 (Scopus). http://dx.doi.org/10.1016/j.ijbiomac.2024.133983

3. Krumova, E., **Benkova, D.**, Stoyancheva, G., Dishliyska, V., Miteva-Staleva, J., Kostadinova, A., Ivanov, K., El-Sayed, Kh., Staneva, G., Elshoky, H. A. (2024). Exploring the mechanism underlying the antifungal activity of chitosan-based ZnO, CuO, and SiO_2 nanocomposites as nanopesticides against *Fusarium solani* and *Alternaria solani*. *International Journal of Biological Macromolecules*, 268, Elsevier, 2024, 131702. SJR (Scopus):1.245, JCR-IF (Web of Science):7.7, Q1 (Scopus). https://doi.org/10.1016/j.ijbiomac.2024.131702

Participation in Scientific Forums:

Participation in International Scientific Forums:

1. **Oral Presentation on topic "Newly synthesized chitosan nanoparticles and chitosan-based nanocomposites as a promising bionanopesticides: A detailed approach of understanding the molecular mechanism of their antifungal activity"**

   D. Benkova, A. Kostadinova, G. Staneva, K. Ivanov, V. Dishliyska, J. Miteva-Staleva, E. Krumova.

   XXXIII INTERNATIONAL ONLINE SCIENTIFIC CONFERENCE, Stara Zagora, Bulgaria, 01 - 02.06.2023.

2. **Poster Presentation on topic "Chitosan-Based Nanomaterials as Promising Bionanopesticides: An Approach of Understanding the Mechanism behind Their Antifungal Activity"**

   D. Benkova, A. Kostadinova, G. Staneva, K. Ivanov, V. Dishliyska, J. Miteva-Staleva, E. Krumova

   Data-Driven Models for Living Systems, Sofia, Bulgaria, 08 - 09.06.2023.

3. **Oral Presentation on topic "Interactions of chitosan-based hybrid nanomaterials with biomimetic models of cell plasma membrane"**

   D. Benkova, A. Kostadinova, H. A. Elshoky, R. Hazarosova, V. Yordanova, G. Staneva

   8th International Symposium on Phospholipids in Pharmaceutical Research, Heidelberg, Germany, 09 - 11.09.2024.

Participation in National Scientific Forums:

4. **Poster presentation on topic "Chitosan-based nanomaterials as nanopesticides against Alternaria solani and Fusarium solani"**

   D. Benkova, A. Kostadinova, G. Staneva, K. Ivanov, V. Dishliyska, J. Miteva-Staleva, E. Krumova

   The Synergy Between Science and Business: Present and Perspectives, Sofia, Bulgaria, 20 - 20.11.2023.

5. **Oral presentation on topic "Antifungal Activity of Chitosan-Based Nanomaterials against Alternaria solani. Can They Be Reliable and Effective Bionanopesticides?"**

   D. Benkova, A. Kostadinova, V. Dishliyska, J. Miteva-Staleva, Y. Yan, Y.-S. Liu, K. Ivanov, G. Staneva, H. Elshoky, E. Krumova

   Fourth Youth Scientific Session "Biomedicine and Quality of Life", Sofia, Bulgaria, 05 - 06.12.2023.

6. **Oral presentation on topic "Chitosan-based hybrid nanomaterials: Interactions with biomimetic membranes"**

   D. Benkova, A. Kostadinova, R. Hazarosova, V. Yordanova, H. A. Elshoky, G. Staneva

   Fourth National Congress of Physic Sciences, Sofia, Bulgaria, 07 - 09.10.2024.

Personal scientific awards related to the dissertation:

1. **Certificate for Excellent Presentation by a Young Scientist**
   Fourth National Congress on Physic Sciences, Sofia, Bulgaria, October 7–9, 2024. Presentation topic: *"Chitosan-Based Hybrid Nanomaterials: Interaction with Biomimetic Membranes"*.
2. **Young Scientists Award "Ivan Evstratiev Geshov"** from the Bulgarian Academy of Sciences Scientific achievement on the topic: *"Bioactivity of Newly Synthesized Chitosan-Based Nanomaterials"*, Scientific Area 4 – Biomedicine and Quality of Life, Sofia, Bulgaria, May 23, 2025.

References:

1. Pokorná, S., Ventura, A. E., Santos, T. C. B., Hof, M., Prieto, M., Futerman, A. H., & Silva, L. C. (2022). Laurdan in live cell imaging: Effect of acquisition settings, cell culture conditions and data analysis on generalized polarization measurements. *Journal of Photochemistry and Photobiology B: Biology*, *228*, 112404. https://doi.org/10.1016/j.jphotobiol.2022.112404

2. Orlikowska-Rzeźnik, H., Krok, E., Chattopadhyay, M., Lester, A., & Piątkowski, L. (2023). Laurdan discerns lipid membrane hydration and cholesterol content. *Journal of Physical Chemistry B, 127*(15), 3382–3391. https://doi.org/10.1021/acs.jpcb.3c00654

3. Rinaudo, M. (2006). Chitin and chitosan: Properties and applications. *Progress in Polymer Science, 31*(7), 603–632. https://doi.org/10.1016/j.progpolymsci.2006.06.001

4. Li, Y., Kröger, M., & Liu, W. K. (2015). Shape effect in cellular uptake of PEGylated nanoparticles: Comparison between sphere, rod, cube and disk. *Nanoscale*, *7*(41), 16631–16646. https://doi.org/10.1039/C5NR02970H

5. Palma-Guerrero, J. A., Lopez-Jimenez, A. J., Pérez-Berná, I.-C., Huang, H.-B., Jansson, J., Salinas, J., Villalaín, N. D., Read, L. V., & Lopez-Llorca, L. V. (2010). Membrane fluidity determines sensitivity of filamentous fungi to chitosan. *Molecular Microbiology*, *75*(5), 1021–1032. https://doi.org/10.1111/j.1365-2958.2009.07039.x

6. Mady, M. M., Darwish, M. M., Khalil, S., & Khalil, W. M. (2009). Biophysical studies on chitosan-coated liposomes. *European Biophysics Journal, 38*(8), 1127–1133. https://doi.org/10.1007/s00249-009-0524-z

7. Wydro, P., Krajewska, B., & Hac-Wydro, K. (2007). Chitosan as a lipid binder: a langmuir monolayer study of chitosan-lipid interactions. *Biomacromolecules*, *8*(8), 2611–2617. https://doi.org/10.1021/bm700453x

8. Gatoo, M. A., Naseem, S., Arfat, M. Y., Dar, A. M., Qasim, K., & Zubair, S. (2014). Physicochemical properties of nanomaterials: implication in associated toxic manifestations. *BioMed Research International*, *2014*, 498420. https://doi.org/10.1155/2014/498420

9. Clogston, J. D., & Patri, A. K. (2011). Zeta potential measurement. *Methods in molecular biology (Clifton, N.J.)*, *697*, 63–70. https://doi.org/10.1007/978-1-60327-198-1_6

10. Rad, I., Khodayari, K., Alijanvand, S. H., & Mobasheri, H. (2015). Interaction of polyethylene glycol (PEG) with the membrane-binding domains following spinal cord injury (SCI): Introduction of a mechanism for SCI repair. *Journal of Drug Targeting*, *23*(1), 79–88. https://doi.org/10.3109/1061186X.2014.956668

11. Jiang, Y., Huo, S., Mizuhara, T., Das, R., Lee, Y. W., Hou, S., Moyano, D. F., Duncan, B., Liang, X. J., & Rotello, V. M. (2015). The Interplay of Size and Surface Functionality on the Cellular Uptake of Sub-10 nm Gold Nanoparticles. *ACS nano*, *9*(10), 9986–9993. https://doi.org/10.1021/acsnano.5b03521

12. Magarkar, A., Dhawan, V., Kallinteri, P., Viitala, T., Elmowafy, M., Róg, T., & Bunker, A. (2014). Cholesterol level affects surface charge of lipid membranes in saline solution. *Scientific reports*, *4*, 5005. https://doi.org/10.1038/srep05005

13. Quemeneur, F., Rinaudo, M., & Pépin-Donat, B. (2008). Influence of polyelectrolyte chemical structure on their interaction with lipid membrane of zwitterionic liposomes. *Biomacromolecules, 9*(8), 2237–2243. https://doi.org/10.1021/bm800400y

14. Contini, C., Hindley, J. W., Macdonald, T. J., Barritt, J. D., Ces, O., & Quirke, N. (2020). Size dependency of gold nanoparticles interacting with model membranes. *Communications chemistry*, *3*(1), 130. https://doi.org/10.1038/s42004-020-00377-y

15. Martin, C. S., Maximino, M. D., Martins, J. F. V. A., Pazin, W. M., & Constantino, C. J. L. (2024). Exploring the effects of silver, silica-coated silver, and gold nanoparticles on lipid vesicles: Insights from LUVs and GUVs. *Journal of Molecular Liquids*, *406*, 125081. https://doi.org/10.1016/j.molliq.2024.125081

16. Liu, J., Kaksonen, M., Drubin, D. G., & Oster, G. (2006). Endocytic vesicle scission by lipid phase boundary forces. *Proceedings of the National Academy of Sciences of the United States of America*, *103*(27), 10277–10282. https://doi.org/10.1073/pnas.0601045103

17. Chookhongkha, N., Sopondilok, T., & Photchanachai, S. (2013). Effect of chitosan and chitosan nanoparticles on fungal growth and chilli seed quality. *Acta Horticulturae*, *973*, 231–237. https://doi.org/10.17660/ActaHortic.2013.973.32

18. Long, L. T., Tan, L. V., Boi, V. N., & Trung, T. S. (2018). Antifungal activity of water-soluble chitosan against *Colletotrichum capsici* in postharvest chili pepper. *Journal of Food Processing and Preservation*, *42*(1), e13339. https://doi.org/10.1111/jfpp.13339

19. Reglinski, T., Elmer, P.A., Taylor, J.T., Wood, P.N., & Hoyte, S.M. (2010). Inhibition of Botrytis cinerea growth and suppression of botrytis bunch rot in grapes using chitosan. *Plant Pathology*, *59*, 882-890. https://doi.org/10.1111/j.1365-3059.2010.02312.xDigital

20. Wu, K., Yan, Z., Wu, Z., Li, J., Zhong, W., Ding, L., Zhong, T., & Jiang, T. (2024). Recent Advances in the Preparation, Antibacterial Mechanisms, and Applications of Chitosan. *Journal of Functional Biomaterials*, *15*(11), 318. https://doi.org/10.3390/jfb15110318

21. He, L., Liu, Y., Mustapha, A., & Lin, M. (2011). Antifungal activity of zinc oxide nanoparticles against Botrytis cinerea and Penicillium expansum. *Microbiological research*, *166*(3), 207–215. https://doi.org/10.1016/j.micres.2010.03.003

22. El-Batal, A. I., El-Sayyad, G. S., Mosallam, F. M., & El-Sayed, M. A. (2020). *Penicillium chrysogenum*-mediated mycogenic synthesis of copper oxide nanoparticles using gamma rays for in vitro antimicrobial activity against some plant pathogens. *Journal of Cluster Science*, *31*(1), 79–90. https://doi.org/10.1007/s10876-019-01619-3

23. González-Merino, A. M., Hernández-Juárez, A., Betancourt-Galindo, R., Ochoa-Fuentes, Y. M., Valdez-Aguilar, L. A., & Limón-Corona, M. L. (2021). Antifungal activity of zinc oxide nanoparticles in *Fusarium oxysporum–Solanum lycopersicum* pathosystem under controlled conditions. *Journal of Phytopathology*, *169*(7–8), 533–544. https://doi.org/10.1111/jph.13023

24. Abdelrhim, A. S., Mazrou, Y. S. A., Nehela, Y., Atallah, O. O., El-Ashmony, R. M., & Dawood, M. F. A. (2021). Silicon Dioxide Nanoparticles Induce Innate Immune Responses and Activate Antioxidant Machinery in Wheat Against *Rhizoctonia solani*. *Plants (Basel, Switzerland)*, *10*(12), 2758. https://doi.org/10.3390/plants10122758

25. Akpinar Ergün, Ilgin & Sar, Taner & Ünal, Muammer. (2017). Antifungal Effects of Silicon Dioxide Nanoparticles (SiO2NPs) against Various Plant Pathogenic Fungi.

26. Sunil, D. (2013). Recent advances on chitosan-metal oxide nanoparticles and their biological application. *Materials Science Forum*, *754*, 99–108. https://api.semanticscholar.org/CorpusID:97560698

27. Malerba, M., & Cerana, R. (2016). Chitosan Effects on Plant Systems. *International Journal of Molecular Sciences*, *17*(7), 996. https://doi.org/10.3390/ijms17070996

28. Feigl, G. (2023). The impact of copper oxide nanoparticles on plant growth: A comprehensive review. *Journal of Plant Interactions*, *18*(1). https://doi.org/10.1080/17429145.2023.2243098

29. Gogos, A., Knauer, K., & Bucheli, T. (2012). Nanomaterials in plant protection and fertilization: Current state, foreseen applications, and research priorities. *Journal of Agricultural and Food Chemistry*, *60*(39), 9781–9792. https://doi.org/10.1021/jf302154y

30. Ouda, S. (2014). Antifungal activity of silver and copper nanoparticles on two plant pathogens, *Alternaria alternata* and *Botrytis cinerea*. *Research Journal of Microbiology*, *9*(1), 34–42. https://scialert.net/abstract/?doi=jm.2014.34.42

31. Yang, W., Wang, L., Mettenbrink, E. M., DeAngelis, P. L., & Wilhelm, S. (2021). Nanoparticle Toxicology. *Annual review of pharmacology and toxicology*, *61*, 269–289. https://doi.org/10.1146/annurev-pharmtox-032320-110338

32. Krishnaraj, C., Ramachandran, R., Mohan, K., & Kalaichelvan, P. T. (2012). Optimization for rapid synthesis of silver nanoparticles and its effect on phytopathogenic fungi. *Spectrochimica acta. Part A, Molecular and biomolecular spectroscopy*, *93*, 95–99. https://doi.org/10.1016/j.saa.2012.03.002

33. Kasprowicz, M., Kozio, M., & Gorczyca, A. (2010). The effect of silver nanoparticles on phytopathogenic spores of *Fusarium culmorum*. *Canadian Journal of Microbiology*, *56*(3), 247–253. https://doi.org/10.1139/w10-012

34. Toodehzaeim, M. H., Zandi, H., Meshkani, H., & Hosseinzadeh Firouzabadi, A. (2018). The Effect of CuO Nanoparticles on Antimicrobial Effects and Shear Bond Strength of Orthodontic Adhesives. *Journal of dentistry (Shiraz, Iran)*, *19*(1), 1–5.

35. Rizvi, S. A. A., & Saleh, A. M. (2018). Applications of nanoparticle systems in drug delivery technology. *Saudi pharmaceutical journal: SPJ: the official publication of the Saudi Pharmaceutical Society*, *26*(1), 64–70. https://doi.org/10.1016/j.jsps.2017.10.012

36. Kasemets, K., Käosaar, S., Vija, H., Fascio, U., & Mantecca, P. (2019). Toxicity of differently sized and charged silver nanoparticles to yeast *Saccharomyces cerevisiae* BY4741: a nano-biointeraction perspective. *Nanotoxicology*, *13*(8), 1041–1059. https://doi.org/10.1080/17435390.2019.1621401

37. Matras, E., Gorczyca, A., Przemieniecki, S. W., & Oćwieja, M. (2022). Surface properties-dependent antifungal activity of silver nanoparticles. *Scientific reports*, *12*(1), 18046. https://doi.org/10.1038/s41598-022-22659-2

38. Lipke, P. N., & Ovalle, R. (1998). Cell wall architecture in yeast: new structure and new challenges. *Journal of bacteriology*, *180*(15), 3735–3740. https://doi.org/10.1128/JB.180.15.3735-3740.1998

39. Chen, L.-C., Kung, S.-K., Chen, H.-H., & Lin, S.-B. (2010). Evaluation of zeta potential difference as an indicator for antibacterial strength of low molecular weight chitosan. *Carbohydrate Polymers*, *82*(3), 913–919. https://doi.org/10.1016/j.carbpol.2010.06.017

40. Lopez-Moya, F., Colom-Valiente, M. F., Martinez-Peinado, P., Martinez-Lopez, J. E., Puelles, E., Sempere-Ortells, J. M., & Lopez-Llorca, L. V. (2015). Carbon and nitrogen limitation increase chitosan antifungal activity in Neurospora crassa and fungal human pathogens. *Fungal biology*, *119*(2-3), 154–169. https://doi.org/10.1016/j.funbio.2014.12.003

41. Jaime, M. D., Lopez-Llorca, L. V., Conesa, A., Lee, A. Y., Proctor, M., Heisler, L. E., Gebbia, M., Giaever, G., Westwood, J. T., & Nislow, C. (2012). Identification of yeast genes that confer resistance to chitosan oligosaccharide (COS) using chemogenomics. *BMC genomics*, *13*, 267. https://doi.org/10.1186/1471-2164-13-267

42. Kim, E., Kang, M., Liu, H., Cao, C., Liu, C., Bentley, W. E., Qu, X., & Payne, G. F. (2019). Pro- and Anti-oxidant Properties of Redox-Active Catechol-Chitosan Films. *Frontiers in chemistry*, *7*, 541. https://doi.org/10.3389/fchem.2019.00541

43. López-Moya, F., Kowbel, D., Nueda, M. J., Palma-Guerrero, J., Glass, N. L., & Lopez-Llorca, L. V. (2016). Neurospora crassa transcriptomics reveals oxidative stress and plasma membrane homeostasis biology genes as key targets in response to chitosan. *Molecular bioSystems*, *12*(2), 391–403. https://doi.org/10.1039/c5mb00649j

44. Roller, S., & Covill, N. (1999). The antifungal properties of chitosan in laboratory media and apple juice. *International journal of food microbiology*, *47*(1-2), 67–77. https://doi.org/10.1016/s0168-1605(99)00006-9

45. Kessler, A., Hedberg, J., Blomberg, E., & Odnevall, I. (2022). Reactive Oxygen Species Formed by Metal and Metal Oxide Nanoparticles in Physiological Media—A Review of Reactions of Importance to Nanotoxicity and Proposal for Categorization. *Nanomaterials*, *12*(11), 1922. https://doi.org/10.3390/nano12111922

46. Lakshmi Prasanna, V., & Vijayaraghavan, R. (2015). Insight into the Mechanism of Antibacterial Activity of ZnO: Surface Defects Mediated Reactive Oxygen Species Even in the Dark. *Langmuir: the ACS journal of surfaces and colloids*, *31*(33), 9155–9162. https://doi.org/10.1021/acs.langmuir.5b02266

47. Attarilar, S., Yang, J., Ebrahimi, M., Wang, Q., Liu, J., Tang, Y., & Yang, J. (2020). The Toxicity Phenomenon and the Related Occurrence in Metal and Metal Oxide Nanoparticles: A Brief Review From the Biomedical Perspective. *Frontiers in bioengineering and biotechnology*, *8*, 822. https://doi.org/10.3389/fbioe.2020.00822

48. Sharma, P., Jha, A. B., Dubey, R., & Pessarakli, M. (2012). Reactive oxygen species, oxidative damage, and antioxidative defense mechanism in plants under stressful conditions. *Journal of Botany*, *2012*, 1–26. https://doi.org/10.1155/2012/217037

49. Ayala, A., Muñoz, M. F., & Argüelles, S. (2014). Lipid peroxidation: Production, metabolism, and signaling mechanisms of malondialdehyde and 4-hydroxy-2-nonenal. *Oxidative Medicine and Cellular Longevity*, *2014*, 360438. https://doi.org/10.1155/2014/360438

50. Repetto, M., Semprine, J., & Boveris, A. (2012). Lipid peroxidation: Chemical mechanism, biological implications and analytical determination. In *Lipid peroxidation*. InTech. https://doi.org/10.5772/45943

51. Akagawa, M. (2021). Protein carbonylation: Molecular mechanisms, biological implications, and analytical approaches. *Free Radical Research*, *55*(4), 307–320. https://doi.org/10.1080/10715762.2020.1851027

52. Fedorova, M., Bollineni, R., & Hoffmann, R. (2014). Protein carbonylation as a major hallmark of oxidative damage: Update of analytical strategies. *Mass Spectrometry Reviews*, *33*(2), 79–97. https://doi.org/10.1002/mas.21381

53. Gilbert, J. L. (2017). Corrosion in the human body: Metallic implants in the complex body environment. *Corrosion*, *73*(12), 1478–1495. https://doi.org/10.5006/2563

54. Dominguez, G. A., Lohse, S. E., Torelli, M. D., Murphy, C. J., Hamers, R. J., Orr, G., & Klaper, R. D. (2015). Effects of charge and surface ligand properties of nanoparticles on oxidative stress and gene expression within the gut of Daphnia magna. *Aquatic toxicology (Amsterdam, Netherlands)*, *162*, 1–9. https://doi.org/10.1016/j.aquatox.2015.02.015

55. Sant, D. G., Tupe, S. G., Ramana, C. V., & Deshpande, M. V. (2016). Fungal cell membrane-promising drug target for antifungal therapy. *Journal of applied microbiology*, *121*(6), 1498–1510. https://doi.org/10.1111/jam.13301

56. Kong, M., Chen, X. G., Xing, K., & Park, H. J. (2010). Antimicrobial properties of chitosan and mode of action: a state-of-the-art review. *International journal of food microbiology*, *144*(1), 51–63. https://doi.org/10.1016/j.ijfoodmicro.2010.09.012

57. Ing, L. Y., Zin, N. M., Sarwar, A., & Katas, H. (2012). Antifungal activity of chitosan nanoparticles and correlation with their physical properties. *International journal of biomaterials*, *2012*, 632698. https://doi.org/10.1155/2012/632698

58. Zakrzewska, A., Boorsma, A., Brul, S., Hellingwerf, K. J., & Klis, F. M. (2005). Transcriptional response of Saccharomyces cerevisiae to the plasma membrane-perturbing compound chitosan. *Eukaryotic cell*, *4*(4), 703–715. https://doi.org/10.1128/EC.4.4.703-715.2005

59. Leroux, P., Fritz, R., Debieu, D., Albertini, C., Lanen, C., Bach, J., Gredt, M., & Chapeland, F. (2002). Mechanisms of resistance to fungicides in field strains of Botrytis cinerea. *Pest management science*, *58*(9), 876–888. https://doi.org/10.1002/ps.566

60. Walker, L. A., Gow, N. A., & Munro, C. A. (2010). Fungal echinocandin resistance. *Fungal genetics and biology: FG & B*, *47*(2), 117–126. https://doi.org/10.1016/j.fgb.2009.09.003

61. Lima, S. L., Colombo, A. L., & de Almeida Junior, J. N. (2019). Fungal Cell Wall: Emerging Antifungals and Drug Resistance. *Frontiers in microbiology*, *10*, 2573. https://doi.org/10.3389/fmicb.2019.02573

62. Song, L., Wang, S., Zou, H., Yi, X., Jia, S., Li, R., & Song, J. (2025). Regulation of ergosterol biosynthesis in pathogenic fungi: Opportunities for therapeutic development. *Microorganisms*, *13*(4), 862. https://doi.org/10.3390/microorganisms13040862

ACKNOWLEDGEMENTS

First and foremost, I would like to express my deep gratitude to my supervisors. I sincerely thank Prof. Dr. Galya Staneva for her invaluable guidance, profound knowledge, and the practical skills acquired in the fields of lipidology, biophysics, and model membranes. I also express my appreciation to Assoc. Prof. Dr. Anelia Kostadinova for providing me the opportunity to work on this topic, for her valuable knowledge and experience in nanotechnology and molecular biology. I am sincerely grateful for your continuous support, trust, and for fostering an environment conducive to my scientific development and growth.

I would also like to extend special thanks to the co-authors who contributed to the realization of this dissertation and the accompanying scientific publications. I am grateful to Assoc. Prof. Dr. Ekaterina Krumova and her team at the Institute of Microbiology "Stefan Angeloff," BAS, for their professionalism, openness to discussions, and productive collaboration. I also thank Dr. Hisham Elshoky and his team at the Central Laboratory of Nanotechnology and Advanced Materials, Agricultural Research Center, Giza, Egypt, for their high professionalism and dedication to our collaborative work.

I am thankful to the "Lipid–Protein Interactions" Section, headed by Prof. Dr. Galya Staneva, for providing access to the laboratory equipment and for the opportunity to gain both theoretical and practical skills. I would like to personally thank Assist. Prof. Dr. Vesela Yordanova for her collegiality and willingness to share knowledge and experience from the very beginning of my academic journey.

I am also grateful to my colleagues in the academy for the excellent working and friendly atmosphere, as well as the fruitful scientific discussions. Last but not least, I wish to express my deepest gratitude to my family and friends for their understanding and support of my scientific ambitions throughout the entire period of my dissertation work.

I would like to acknowledge the following projects for their financial support of the experimental work, scientific publications, and participation in scientific forums related to my dissertation:

(1) Bilateral international collaboration between the Institute of Biophysics and Biomedical Engineering, BAS, and the ASRT and Nanotechnology and Advanced Materials Central Lab, Agricultural Research Centre, Egypt, on the topic "Biological Activity of Nanocomposite Materials with Potential Medical and Microbiology Applications" – consumables and publications.

(2) D01-183/2022 "National Center for Biomedical Photonics," part of the National Roadmap for Scientific Infrastructure 2020–2027 – laboratory equipment.

(3) KP-06-N77/13 Investigation of Motor and Physiological Activity through Biocompatible and Antibacterial Multimodal Sensors, 2023–2027 – conferences and publications.

I also express my gratitude to the Ministry of Education and Science, National Research Program "Young Scientists and Postdoctoral Researchers – 2," Module "Young Scientists," for financial support

under the project "Biological Activity of Chitosan-Based Nanomaterials with Potential Biomedical and Agrobiological Applications."